AFRL-RV-PS-
TR-2021-0016

AFRL-RV-PS-
TR-2021-0016

P AND S VELOCITY MODELS FOR THE MIDDLE EAST FROM A NEW ALGORITHM OF JOINT INVERSION OF BODY AND SURFACE WAVE TRAVEL TIMES AND RECEIVER FUNCTIONS

Xiaoxi Ni, et al.

Array Information Technology
7474 Greenway Center Drive, Suite 600
Greenbelt, MD 20770

01 December 2020

Final Report

AIR FORCE RESEARCH LABORATORY
Space Vehicles Directorate
3550 Aberdeen Ave SE
AIR FORCE MATERIEL COMMAND
KIRTLAND AIR FORCE BASE, NM 87117-5776

DTIC COPY

NOTICE AND SIGNATURE PAGE

AFRL-RV-PS-TR-2021-0016 HAS BEEN REVIEWED AND IS APPROVED FOR PUBLICATION IN ACCORDANCE WITH ASSIGNED DISTRIBUTION STATEMENT.

//SIGNED//	//SIGNED//
Dr. Frederick R. Schult	Erin N. Pettyjohn, Chief
Program Manager, AFRL/RVBN	AFRL Geospace Technologies Division

REPORT DOCUMENTATION PAGE

Form Approved
OMB No. 0704-0188

1. REPORT DATE *(DD-MM-YYYY)*	**2. REPORT TYPE**	**3. DATES COVERED** *(From - To)*
01-12-2020	Final Report	01 Feb 2017 – 01 Nov 2020

4. TITLE AND SUBTITLE
P and S Velocity Models for the Middle East from a New Algorithm of Joint Inversion of Body and Surface Wave Travel Times and Receiver Functions

5a. CONTRACT NUMBER
FA9453-17-C-0028

5b. GRANT NUMBER

5c. PROGRAM ELEMENT NUMBER
62601F

6. AUTHOR(S)
Xiaoxi Ni, Hafidh Ghalib, Haijiang Zhang

5d. PROJECT NUMBER
1010

5e. TASK NUMBER
EF129472

5f. WORK UNIT NUMBER
V136

7. PERFORMING ORGANIZATION NAME(S) AND ADDRESS(ES)
Array Information Technology
7474 Greenway Center Drive, Suite 600
Greenbelt, MD 20770

8. PERFORMING ORGANIZATION REPORT NUMBER

9. SPONSORING / MONITORING AGENCY NAME(S) AND ADDRESS(ES)
Air Force Research Laboratory
Space Vehicles Directorate
3550 Aberdeen Avenue SE
Kirtland AFB, NM 87117-5776

10. SPONSOR/MONITOR'S ACRONYM(S)
AFRL/RVBN

11. SPONSOR/MONITOR'S REPORT NUMBER(S)
AFRL-RV-PS-TR-2021-0016

12. DISTRIBUTION / AVAILABILITY STATEMENT
Approved for public release; distribution is unlimited. (AFMC-2021-1183 dtd 14 Apr 2021)

13. SUPPLEMENTARY NOTES

14. ABSTRACT
This study is aimed at collecting and processing digital waveforms and bulletin data from seismic networks in the Middle East and performing a joint inversion of five data types including absolute body wave travel times, differential body wave travel times, surface wave dispersion between station and event pairs, surface wave dispersion between station pairs from ambient noise cross-correlation, and receiver functions for better constraint on the P and S velocity models for the Middle East. We have collected and processed waveform and bulletin data and constructed a phase picks database for the region. We have also processed ambient noise data and performed waveform cross-correlation to extract empirical Green's functions and measured Rayleigh wave dispersions. Surface wave dispersions between earthquakes and stations are also measured. Teleseismic waveforms are processed for receiver function analysis in the region. A joint tomographic inversion of the processed datasets is performed for high-resolution P and S velocity models for the Middle East. The obtained velocity models show complex features that are in general agreement with the regional tectonics. Resolution analysis indicates that data coverage is sufficient, and tomographic resolution is adequate for the study area. The event relocations from the inversion are also utilized to construct a GT5 database for the region.

15. SUBJECT TERMS
joint tomographic inversion, double-difference tomography, absolute and differential body wave travel times, surface wave dispersion, ambient noise cross-correlation, receiver functions

16. SECURITY CLASSIFICATION OF:			**17. LIMITATION OF ABSTRACT**	**18. NUMBER OF PAGES**	**19a. NAME OF RESPONSIBLE PERSON**
a. REPORT	**b. ABSTRACT**	**c. THIS PAGE**			Dr. Frederick R. Schult
Unclassified	Unclassified	Unclassified	Unlimited	72	**19b. TELEPHONE NUMBER** *(include area code)*

This page is intentionally left blank.

Table of Contents

Page

List of Figures

Page

Page

Page

Page

List of Tables

Page

This page is intentionally left blank.

1. SUMMARY

This study is aimed at collecting and processing digital waveforms and bulletin data from seismic networks in the Middle East and performing a joint inversion of five data types including absolute body wave travel times, differential body wave travel times, surface wave dispersion between station and event pairs, surface wave dispersion between station pairs from ambient noise cross-correlation, and receiver functions for better constraint on the P and S velocity models for the Middle East. We have collected seismic data for 11,219 events from 2006 to 2010 recorded by deployments and regional seismic networks in the Middle East including the NISN, KSIRS, ISN and IRSC networks and performed analysis including phase picking, association, and relocation. Quality control is performed, and abnormal arrivals are eliminated to ensure quality of the data. We have obtained 87,395 P and 69,144 S phase picks after quality control. To improve coverage of the study area, we have also collected and processed bulletin data from other sources in the Middle East. We retrieved 18 earthquake clusters from the GCCEL database and processed phase pick data of 1,620 seismic events recorded by 1,476 seismic stations in the Middle East. Additional bulletin data from the networks in Jordan, Israel, Saudi Arabia, Syria, UAE, Oman, and Yemen have also been collected and processed. We have processed ambient noise data from continuous recordings from the NISN, KSIRS and ISN networks from 2009 to 2010. We process the ambient noise data including single station data preparation, cross-correlation and temporal stacking, and measurement of dispersion curves. Rayleigh wave phase and group velocity dispersions from 121 pairs of seismic stations in the Middle East are obtained. We have also measured surface wave dispersion between earthquakes and stations in the Middle East. The MFT technique is adopted to measure Rayleigh wave group velocity dispersion on the seismograms. We have processed seismic recordings from 256 events from 2001 to 2009 and obtained 2,988 Rayleigh wave group velocity dispersion curves. We have also conducted receiver function analysis in the study area and obtained receiver functions at 25 stations. With the processed data, we have performed a joint inversion of body wave travel times, surface dispersions and receiver functions for high-resolution P and S velocity models for the Middle East. The study area is set in a region from latitudes 10ºN to 45ºN, and longitudes 30ºE to 65ºE. We divide the study area into 0.5ºx0.5º cells horizontally. In the vertical direction, we set up layers at 5km intervals from the Earth surface to the depth of 60km, and additional layers at 80, 120 and 210km. We select 12,437 events recorded by 1,647 stations from the phase picks database that we have constructed for the region. The body wave data include 178,633 first P arrivals, 70,505 first S arrivals, 100,513 differential P arrivals, and 42,519 differential S arrivals. We also adopt Rayleigh wave group velocity dispersions measured in the Middle East. The surface wave data include 95,811 Rayleigh wave group velocity measurements from 256 events recorded by 39 stations in the periods from 2 to 100s. We also include Rayleigh wave group velocity dispersions measured from ambient noise cross-correlation from 121 station pairs in the region. Receiver functions obtained at 25 stations in the region are also utilized. We run the inversion iteratively and invert for velocity models and event relocations simultaneously. The obtained velocity models show complex features that are in general agreement with the regional tectonics. We have performed resolution analysis of the tomography results. Derivative weighted sum (DWS) distributions for P and S waves implies that ray densities are sufficient for the study area. The checkerboard test results indicate that the resolution of the tomographic inversion is adequate for most of the study area. We have also utilized the event relocations from the tomographic inversion to construct a high-quality GT5 database of 396 events for the Middle East.

2. INTRODUCTION

One of the fundamental problems facing location of earthquakes and explosions is creating accurate structure models for the Earth. Using a high-resolution three-dimensional velocity model significantly improves seismic event location accuracy [1-2] and thus helps to satisfy the goal of nuclear explosion monitoring. Crustal and upper mantle velocity models are not only key for accurately predicting travel-times, but also essential for modeling surface-wave dispersion and full waveforms at regional distances. Seismic tomography using body wave or surface wave data has been widely used in investigating structures of the Earth at local, regional, and global scales [3-5]. Ray-based travel time tomography using body-wave travel times has been popular and effective because of its simplicity in theory and low computational requirements. However, it has drawbacks besides its high frequency approximation. Shallow structures near the Earth surface generally cannot be well resolved from body wave travel time tomography due to lack of crossing seismic rays. Also, S-wave observations are often contaminated by P-wave coda or other converted phases, thus Vs models from tomographic inversion of S-wave travel times tend to have lower resolution and greater uncertainty than the Vp models. Surface-wave tomography based on ambient noise data has been widely used to investigate regional crustal structure in the past decade using a period band of 5-40s [6-7]. Recent studies show that shorter period surface waves can also be retrieved from ambient noise cross-correlation [8-9]. Shorter period surface waves are more sensitive to the near-surface velocity variations and are thus particularly useful to resolve shallow structures.

Due to nonlinearity and non-uniqueness associated with geophysical modeling, velocity models inverted from different datasets are often not consistent with each other. Each data type has unique sensitivity to the Earth media, e.g. receiver functions are mainly sensitive to shear wave velocity contrasts and vertical travel times, whereas surface wave dispersion measurements are sensitive to vertical shear wave velocity averages, and relatively insensitive to sharp velocity contrasts. One way to improve the reliability of the velocity models is to use multiple datasets, especially different data types, to better constrain the velocity models. Joint inversions based on both body wave and surface wave data provide more constraints on the velocity structures and thus yield more accurate and reliable velocity models at global, regional, and local scales [10-12]. Joint inversion of receiver functions and surface wave dispersion is commonly used in investigation of crustal and upper mantle velocity structures; however, the technique is generally utilized to derive Vs models, but Vp models are not well constrained. Fang et al. (2016) [13] developed a new joint inversion method to invert body wave travel times and surface wave dispersion data for Vp and Vs models simultaneously. The technique combines the double difference (DD) inversion method for body wave travel times and the one-step inversion method of surface wave dispersion of Fang et al. (2015) [14]. The method incorporates sensitivity of surface wave dispersion with respect to Vp in addition to Vs and improves the Vs model and shallow Vp model at the same time due to the fact that short-period Rayleigh wave measurements have relatively large sensitivity to Vp in shallow crust. Fang et al. (2016) [13] applied the joint inversion method to body wave travel times and Rayleigh wave group velocity dispersion data from ambient noise cross-correlation in the Southern California Plate Boundary Region and obtained new Vp and Vs models for the region. Checkerboard tests of the results show improved Vp and Vs resolution over the models obtained from inversion of body wave travel times or surface wave dispersion data alone. Synthetic seismograms calculated based on the velocity models from the joint inversion also show better

correlation with the observation data in both phase and amplitude than those from the current SCEC model.

Under this study, we extend the technique to a joint inversion of five data types for better constraint on the velocity model. The objectives of this study are to develop a new algorithm of joint inversion of body and surface wave travel times and receiver functions and utilize a data collection from long-term deployments and regional seismic networks in the Middle East to perform a tomographic inversion for three-dimensional high-resolution P and S wave velocity models for the region. Both absolute and differential body wave travel times, surface wave dispersion from both earthquakes and ambient noises, and receiver functions are measured and utilized for multi-data type coverage of the study area and thus have better constraints in the inversion and yield more reliable and robust velocity models for the region.

3. METHODS, ASSUMPTIONS, AND PROCEDURES

3.1. DOUBLE-DIFFERENCE TOMOGRAPHY OF ABSOLUTE AND DIFFERENTIAL BODY WAVE TRAVEL TIMES

Double-difference tomography developed by Zhang and Thurber (2003) [4] is a generalization of the DD location technique of Waldhauser and Ellsworth (2000) [15]. It uses both absolute and differential body wave arrival times in a joint solution for event locations and velocity structures. Relative times are more accurate than absolute times alone. This method recovers more accurate event locations and velocity structures near the source region than standard tomography, and sharpens the velocity image in the source region due to combination of higher accuracy of differential time data and concentration of corresponding model derivatives in the source region. The latter results from cancellation of model derivative terms where ray paths overlap away from the source region. DD tomography can be applied to both local and regional scale problems. Zhang and Thurber (2003) [4] demonstrated the advantages of DD tomography on the Hayward fault, California as well as the subduction zone of northern Honshu, Japan [16], illustrating the strength of the method at a variety of scales.

The DD tomography was originally implemented for local-scale problems in Cartesian coordinate system, and was later modified by introducing the "sphere-in-a-box" technique in which a spherical Earth is placed in a rectangular box for calculation. The "sphere-in-a-box" version of DD tomography takes into account the curvature of the Earth surface, thus can be applied to larger regional problems, but the calculation is still performed in a Cartesian coordinate system. In recent development of the DD tomography, the calculation is implemented in a spherical coordinate system that accounts for the Earth curvature natively. A spherical-Earth finite-difference (SEFD) travel time method is used to calculate travel times and trace rays. The basic concept is an extension of the standard Cartesian finite-difference (FD) travel time algorithm to the spherical case through development of a mesh in radius, co-latitude, and longitude, expression of the FD derivatives in a form appropriate to the spherical mesh, and the construction of "stencils" to calculate extrapolated travel times. To improve the accuracy and efficiency of the ray tracing, a hybrid approach is adopted. First, the FD method with a coarser grid interval is utilized to calculate an approximate ray path. Next this approximate ray path is bent with the spherical pseudo-bending approach of Koketsu and Sekine (1998) [17] until it converges to the desired accuracy.
The linearized DD tomography equation can be written in a matrix form [18] as:

$$\begin{bmatrix} \mathbf{G}_{\mathrm{H}}^{\mathrm{Tp}} & \mathbf{G}_{\mathrm{V_p}}^{\mathrm{Tp}} & 0 \\ \mathbf{G}_{\mathrm{H}}^{\mathrm{Ts}} & 0 & \mathbf{G}_{\mathrm{V_s}}^{\mathrm{Ts}} \end{bmatrix} \begin{bmatrix} \mathbf{\Delta H} \\ \mathbf{\Delta m_p} \\ \mathbf{\Delta m_s} \end{bmatrix} = \begin{bmatrix} \mathbf{d}^{\mathrm{Tp}} \\ \mathbf{d}^{\mathrm{Ts}} \end{bmatrix} \tag{1}$$

where $\mathbf{G}_{\mathrm{H}}^{\mathrm{Tp}}$, $\mathbf{G}_{\mathrm{H}}^{\mathrm{Ts}}$, $\mathbf{G}_{\mathrm{V_p}}^{\mathrm{Tp}}$, $\mathbf{G}_{\mathrm{V_s}}^{\mathrm{Ts}}$ are the sensitivity matrices of first P and S travel times with respect to the hypocenter parameters, P-wave velocity (Vp), and S-wave velocity (Vs), respectively; $\mathbf{\Delta H}$, $\mathbf{\Delta m_p}$, $\mathbf{\Delta m_s}$ are perturbations to hypocenter parameters, Vp, and Vs model parameters; and $\mathbf{d}^{\mathrm{Tp}}$ and $\mathbf{d}^{\mathrm{Ts}}$ are residuals for absolute or differential P and S travel times.

3.2. ONE-STEP SURFACE WAVE TOMOGRAPHY

Ambient noise carries information about the Earth media, and it is demonstrated that ambient-noise cross-correlation can be used to retrieve surface wave Green's functions between station pairs [19]. The obtained surface wave Green's functions can be utilized to invert for 3D Earth structures [6]. High-frequency surface waves are generally more sensitive to shallow structures, whereas low-frequency surface waves are more sensitive to deeper structures. Thus, surface waves at different periods can be used to recover velocity structures at different depths.

Fang et al. (2015) [14] developed a one-step inversion method to invert surface wave dispersion measurements directly for 3-D variations in velocity without the intermediate step of constructing phase or group velocity maps in the inversion calculation. The fast-marching method (FMM) [20] is used to compute surface wave ray paths and travel times at each period, which avoid the assumption of great circle propagation. The travel time perturbation at each angular frequency ω with respect to a reference model for the path i is given by

$$\delta t_i(\omega) = t_i^{obs}(\omega) - t_i(\omega) \approx -\sum_{k=1}^{K} v_{ik} \frac{\delta C_k(\omega)}{C_k^2(\omega)} \tag{2}$$

where $t_i^{obs}(\omega)$ is the observed surface wave travel time, $t_i(\omega)$ is the calculated travel time from a reference model that can be updated in the inversion, v_{ik} is the bilinear interpolation coefficients along the ray path associated with the ith travel time data and the phase (or group) velocity $C_k(\omega)$ and its perturbation $\delta C_k(\omega)$ of the kth 2-D surface grid point at the angular frequency ω, respectively. Using 1-D depth kernels of Rayleigh wave phase or group velocity data to compressional velocity (Vp), shear velocity (Vs), and density (ρ) at each surface grid node, we can rewrite equation (2) as

$$\delta t_i(\omega) = \sum_{k=1}^{K} -\left(\frac{v_{jk}}{C_k^2}\right) \sum_{j=1}^{J} \left[\left.\frac{\partial C_k(\omega)}{\partial V_{pk}(Z_j)}\right|_{\Theta_k} \partial V_{pk}(Z_j) + \left.\frac{\partial C_k(\omega)}{\partial V_{sk}(Z_j)}\right|_{\Theta_k} \partial V_{sk}(Z_j) + \left.\frac{\partial C_k(\omega)}{\partial \rho_k(Z_j)}\right|_{\Theta_k} \partial \rho_k(Z_j) \right] \tag{3}$$

where Θ_k represents the 1-D reference model at the kth surface grid point on the surface and $V_{pk}(Z_j)$, $V_{sk}(Z_j)$, and $\rho_k(Z_j)$ are the compression velocity, shear velocity, and mass density at the jth depth grid node, respectively. J is the number of grid points in the depth direction, and the number of total grid points of the 3-D model is N = KJ. The linearized equation of one-step surface

wave inversion can be written as

$$\begin{bmatrix}\mathbf{G}_{V_p}^{SW} & \mathbf{G}_{V_s}^{SW} & \mathbf{G}_{\rho}^{SW}\end{bmatrix}\begin{bmatrix}\Delta\mathbf{m_p}\\ \Delta\mathbf{m_s}\\ \Delta\boldsymbol{\rho}\end{bmatrix}=\mathbf{d}^{SW} \tag{4}$$

where $\mathbf{G}_{V_p}^{SW}$, $\mathbf{G}_{V_s}^{SW}$, and $\mathbf{G}_{\rho}^{SW}$ are sensitivity matrices of surface wave travel times with respect to Vp, Vs, and density, respectively; $\Delta\mathbf{m_p}$, $\Delta\mathbf{m_s}$, and $\Delta\boldsymbol{\rho}$ are perturbations to Vp, Vs, and density; and $\mathbf{d}^{SW}$ is the surface wave travel time residuals at different periods. An empirical polynomial relationship between Vp and density [21] can be used to relate the sensitivity of surface wave data with respect to density to Vp. As a result, equation (4) can be rewritten as

$$\begin{bmatrix}\mathbf{G}_{V_p}^{SW}+R_{\rho}\mathbf{G}_{\rho}^{SW} & \mathbf{G}_{V_s}^{SW}\end{bmatrix}\begin{bmatrix}\Delta\mathbf{m_p}\\ \Delta\mathbf{m_s}\end{bmatrix}=\mathbf{d}^{SW} \tag{5}$$

Where $R_{\rho}=\sum_n nX_nV_p^{n-1}$ and X_n represent the fitting polynomial coefficients between Vp and density.

3.3. JOINT INVERSION OF BODY AND SURFACE WAVE TRAVEL TIMES

With the above formulations it is straightforward to combine the surface wave data with the body wave data into a single framework. Specifically, equations (1) and (5) are combined into a single matrix for joint inversion as follows:

$$\begin{bmatrix}\mathbf{G}_H^{T_p} & \mathbf{G}_{V_p}^{T_p} & 0\\ \mathbf{G}_H^{T_s} & 0 & \mathbf{G}_{V_s}^{T_s}\\ 0 & \alpha\left(\mathbf{G}_{V_p}^{SW}+R_{\rho}\mathbf{G}_{\rho}^{SW}\right) & \alpha\mathbf{G}_{V_s}^{SW}\end{bmatrix}\begin{bmatrix}\mathbf{\Delta H}\\ \mathbf{\Delta m_p}\\ \mathbf{\Delta m_s}\end{bmatrix}=\begin{bmatrix}\mathbf{d}^{T_p}\\ \mathbf{d}^{T_s}\\ \alpha\mathbf{d}^{SW}\end{bmatrix} \tag{6}$$

Where α is the weight used to balance the two data types to prevent the results from being dominated by either one. Choosing an appropriate weight between the two data sets is nontrivial, however, due to the fact that they are sensitive to different parts of the model space and the noise levels for different data types are different and in most cases unknown. This can be addressed by using the variances of the two data sets to normalize the objective function to avoid one data set controlling the joint inversion [22-23]. For our joint inversion scheme, we need to estimate the data variances of the two data sets and then normalize them.

Moreover, the joint inversion system in equation (6) is generally ill conditioned. We adopt a smoothing regularization method to stabilize the inversion [24]. In addition, because the Vp/Vs ratio model derived from the Vp and Vs models could vary greatly beyond reasonable ranges, we also add a constraint on the Vp/Vs ratio. The regularized inversion system is as follows:

$$\begin{bmatrix} \mathbf{G}_H^{T_p} & \mathbf{G}_{V_p}^{T_p} & 0 \\ \mathbf{G}_H^{T_s} & 0 & \mathbf{G}_{V_s}^{T_s} \\ 0 & \alpha\left(\mathbf{G}_{V_p}^{SW} + R_\rho \mathbf{G}_\rho^{SW}\right) & \alpha\mathbf{G}_{V_s}^{SW} \\ 0 & \beta_1\mathbf{L} & 0 \\ 0 & 0 & \beta_2\mathbf{L} \\ 0 & \beta_3\mathbf{I} & -\beta_3\eta\mathbf{I} \end{bmatrix} \begin{bmatrix} \mathbf{\Delta H} \\ \mathbf{\Delta m_p} \\ \mathbf{\Delta m_s} \end{bmatrix} = \begin{bmatrix} \mathbf{d}^{T_p} \\ \mathbf{d}^{T_s} \\ \alpha\mathbf{d}^{SW} \\ 0 \\ 0 \\ \beta_3\eta\mathbf{m_s} - \beta_3\mathbf{m_p} \end{bmatrix} \tag{7}$$

Where L is the model smoothing operator, and β_1, β_2, and β_3 are the weighting parameters balancing data fitting and model regularization terms, respectively. L is usually chosen as the first- or second-order spatial derivative operator and $\mathbf{m}_s$, $\mathbf{m}_p$ are the Vs and Vp models from a previous iteration, and η is the reference Vp/Vs ratio. Note that the last row in equation (7) is basically ($\mathbf{m}_p + \Delta\mathbf{m}_p$) = ($\mathbf{m}_s + \Delta\mathbf{m}_s$), which prevents Vp/Vs from becoming unrealistically small or large; η can be chosen based on a priori information about Vp/Vs in the study area. β_1, β_2, and β_3 can be chosen using the L-curve method [24]. Equation (7) is solved for model perturbations $\mathbf{\Delta M}$ ($\mathbf{\Delta H}$, $\mathbf{\Delta m}_p$, $\mathbf{\Delta m}_s$) using the LSMR algorithm, which is based on Golub-Kahan bidiagonalization and can converge faster than the commonly used LSQR [25]. Then the new reference model $\mathbf{M}_{i+1}$ can be obtained by

$$\mathbf{M}_{i+1} = \mathbf{M}_i + \mathbf{\Delta M} \tag{8}$$

which is used for computing surface wave phase or group velocity maps and updating new ray paths for surface waves at each period. The body wave paths are also updated from the newly obtained velocity model. The process is repeated until further reduction of the residual variances for both data sets is insignificant.

Fang et al. (2016) [13] applied the joint inversion method to study crustal and upper mantle structures in the Southern California Plate Boundary Region and obtained new P and S velocity models for the region. Checkerboard tests revealed that the joint inversion of body waves and surface waves yields better resolution than body waves or surface waves alone. Synthetic seismograms calculated based on the velocity models from the joint inversion also show better correlation with the observation data in both phase and amplitude than those from the current SCEC model with the highest improvement in correlation coefficients at nearly 14%, illustrating the effectiveness of the new joint inversion technique in obtaining better velocity models for event relocation and amplitude correction.

3.4. JOINT INVERSION OF BODY AND SURFACE WAVE TRAVEL TIMES AND RECEIVER FUNCTIONS

Under this study, we extend the joint inversion method of Fang et al. (2016) [13] to include receiver functions to further improve the constraints and yield more robust and reliable P and S velocity models. Receiver functions are converted phases generated by underlying seismic discontinuities from incoming teleseismic P-wave or S-wave and their relative delay times are very sensitive to S-wave velocity contrasts. Teleseismic receiver functions have been routinely used to estimate lithospheric structure [26]. The rationale behind the receiver functions technique is to take

advantage of repetitive waveform features of three-component seismograms and isolating the shear-wave response of the crust and upper mantle beneath the recording station. While receiver functions are sensitive to contrasts in seismic velocities, they are weakly sensitive to absolute velocities. It has been shown that if receiver functions are jointly inverted with surface wave dispersion, it can provide a better estimate of the overall velocity structure [26-27].

To jointly invert body and surface wave travel times and receiver functions, we introduce receiver functions in equation (7) and rewrite it as follows:

$$\begin{bmatrix} \mathbf{G}_H^{T_p} & \mathbf{G}_{V_p}^{T_p} & 0 \\ \mathbf{G}_H^{T_s} & 0 & \mathbf{G}_{V_s}^{T_s} \\ 0 & \alpha\left(\mathbf{G}_{V_p}^{SW} + R_\rho \mathbf{G}_\rho^{SW}\right) & \alpha\,\mathbf{G}_{V_s}^{SW} \\ 0 & 0 & \gamma \mathbf{G}_{V_s}^{rf} \\ 0 & \beta_1 \mathbf{L} & 0 \\ 0 & 0 & \beta_2 \mathbf{L} \\ 0 & \beta_3 \mathbf{I} & -\beta_3 \eta \mathbf{I} \end{bmatrix} \begin{bmatrix} \mathbf{\Delta H} \\ \mathbf{\Delta m_p} \\ \mathbf{\Delta m_s} \end{bmatrix} = \begin{bmatrix} \mathbf{d}^{T_p} \\ \mathbf{d}^{T_s} \\ \alpha\,\mathbf{d}^{SW} \\ \gamma \mathbf{d}^{rf} \\ 0 \\ 0 \\ \beta_3 \eta \mathbf{m_s} - \beta_3 \mathbf{m_p} \end{bmatrix} \tag{9}$$

where $\mathbf{G}_{V_s}^{rf}$ is the sensitivity of receiver functions with respect to V_s and γ is a weighting factor used to balance the data types to prevent the results from being dominated by either one, and the other parameters have the same meaning as in Equation (7). Similar to Fang et al. (2016) [13], the weighting factors can be chosen based on the variances of each data type and Equation (9) can be solved iteratively using the LSMR algorithm.

4. STUDY AREA

We focus our study on the Middle East region that encompasses three major seismically active tectonic units: the Arabian plate, Iranian and Turkish plateaus (Figure 1). Interaction between the Arabian, Eurasian, African and Indian plates is the primary force defining the present-day seismotectonic framework of the Middle East. Interplate seismicity is significantly more dominant than the intraplate activity. The plate margin seismicity is associated with a variety of boundaries that range from spreading zones through the Gulf of Aden and the Red Sea, transform faulting along the Dead Sea and East Anatolia of the Turkish plateau, the Bitlis Suture in eastern Turkey, the northwest-southeast trending Zagros thrust zone, the Makran east-west trending continental margin and subduction zone, and the Owen fracture zone in the Arabian Sea.

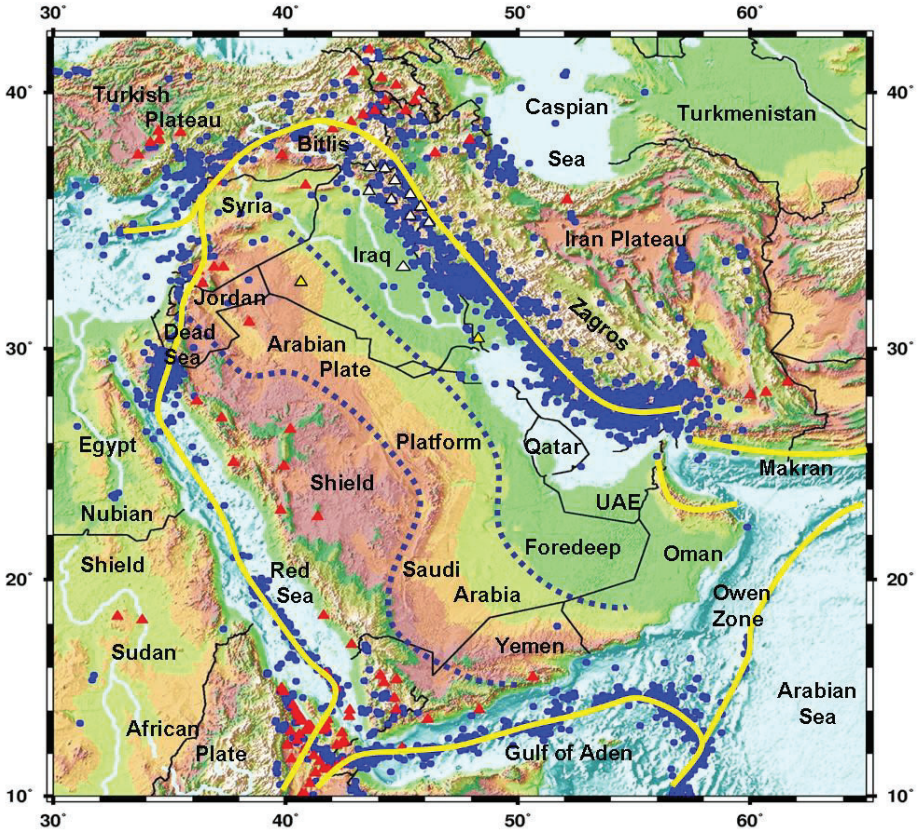

Figure 1. Tectonic settings in the Middle East including physiographic units (dotted lines), plate boundaries (yellow solid lines), seismicity (blue dots) and volcanoes (red triangles).

Researchers from AIT have performed extensive studies on tectonic structures in the Middle East [28-30]. Ghalib et al. (2010) [29] mapped the three-dimensional shear-wave velocity variation using surface waves recorded by the broadband stations of NISN, re-established ISN, and local stations of the Global Seismographic Network (GSN). Analysis of the seismograms netted a new seismicity map for the region consisting of about 2000 well located small to medium size earthquakes using all available phase arrivals including those published by the neighboring Syrian, Iranian and Turkish networks. Analysis of Rayleigh wave pure-path dispersion curves produced detailed maps showing the lateral and vertical variation of seismic velocities throughout the Middle East (Figure 2). These maps show a thick (10-15km) sedimentary layer that overlay the crystalline basement and a Conrad and Moho discontinuities at depths of 20-25km and 45-55km, respectively. The maps also show that the Arabian plate exhibits higher shear-wave velocities than found across the Turkish and Iranian plateaus; imprint of the Zagros Mountain roots extend down as deep as the Moho; and that the tectonic boundaries along the Dead Sea, Taurus and Zagros are more pronounced with depth describing a 60km or thicker Arabian plate.

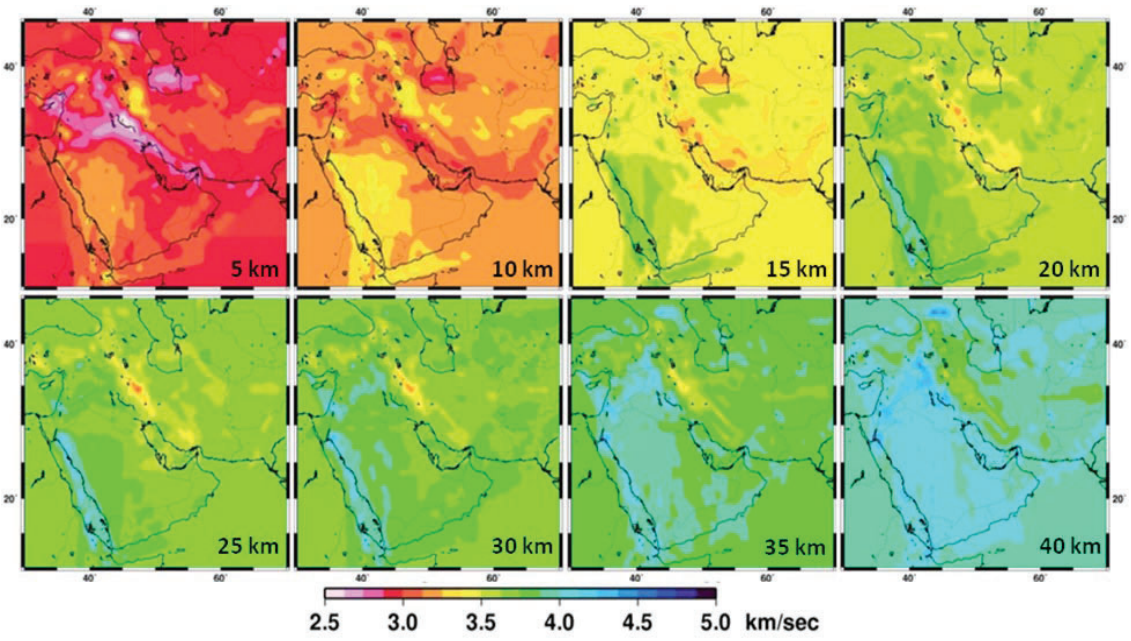

Figure 2. Crustal and upper mantle shear wave velocity model derived from surface wave tomography in the Middle East by Ghalib et al. (2010) [29].

5. RESULTS AND DISCUSSION

5.1. PROCESSING OF WAVEFORMS OF EARTHQUAKES IN THE MIDDLE EAST

We processed and analyzed seismic data of earthquakes recorded by deployments and regional seismic networks in the Middle East. The seismic deployments utilized in this study include the North Iraq Seismographic Network (NISN) and KSIRS Array. NISN was installed by AIT scientists in 2005 when a network of ten broadband seismic stations was deployed in stages over a period of nine months throughout northern, northeastern and central Iraq. Following the unprecedented success of NISN, AIT installed in 2008 the five-element seismo-acoustic array KSIRS to complement and enhance the monitoring capability of the network. The spatial distribution covers a large portion of the folded and foothill zones west of the Zagros continental collision boundary of the Arabian plate. The three-component digital seismic stations of NISN have since been recording continuously at a rate of 100 sps, yielding a rapidly growing database of numerous high quality local and regional events that are characteristic of this relatively young and exceedingly active seismotectonic region. All of NISN and KSIRS stations are equipped with three-component broadband Streckeisen STS-2 seismometers. NISN stations are also equipped with Quanterra 24-bits Q330 digitizers and 20 Gigabytes PB14f Packet Baler data recording system. KSIRS stations are equipped with 26-bits Q330HR digitizers, 8 Gigabytes Marmot field data acquisition with embedded Antelope software, spread spectrum 2.4 GHz radios and with a very small aperture terminal satellite communication system transmitting the data in real-time to Sulaymaniyah and Erbil seismological observatories. The current status of the NISN network and other stations in the Iraq Seismic Network (ISN) are shown in Figure 3. The KSIRS array configuration is shown in Figure 4.

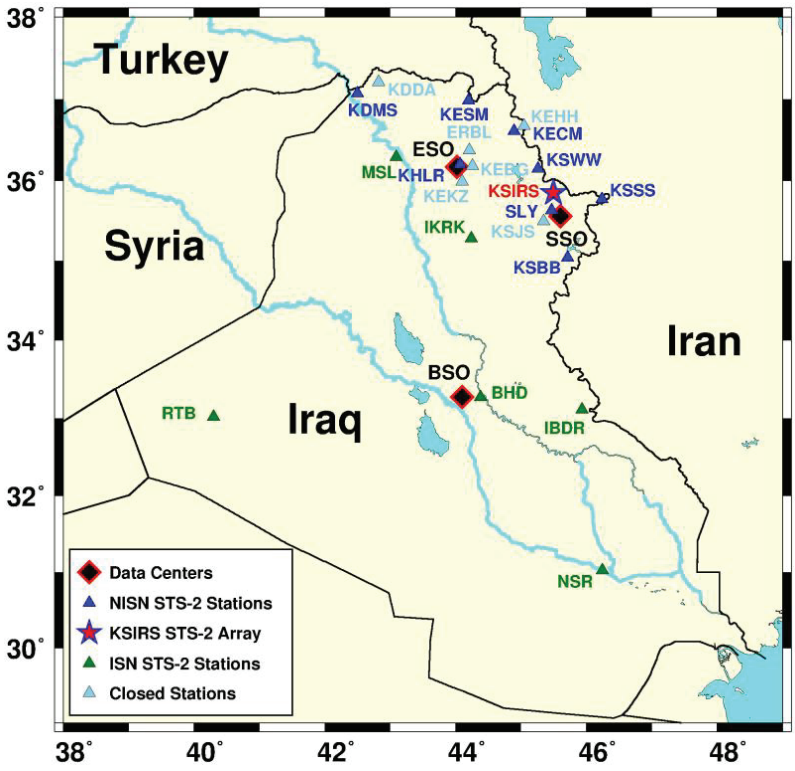

Figure 3. Available seismic stations in Iraq include stations of NISN (blue), KSIRS array (red star) and the refurbished ISN (green). *Shown also are the data centers and closed stations (light blue) in the region.*

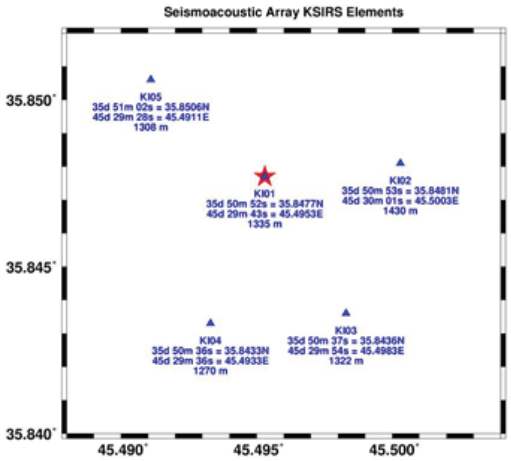

Figure 4. KSIRS array elements configuration, coordinates and elevation. *The blue triangles refer to the location of the array element stations and the red star the array center where all data communication occurs.*

In addition to the NISN and KSIRS data, we also collected supplementary arrivals and waveform data from 67 stations of the Iranian Seismological Center (IRSC) and arrivals only for as many as 131 stations of the ISK network of Kandilli, Turkey.

Prior to manual analysis, we perform automatic processing of the continuous NISN and KSIRS waveform data to generate the initial database. Several **Antelope** routines combined with scripts are used to produce the CSS3.0 tables necessary for manual analysis with the **dbloc2** program. First, a detection table is output using **dbdetect** which is based on a STA/LTA algorithm using selected filter bands. Then the detection table is input to the automatic association routine **dbgrassoc** which utilizes a user defined travel time grid (**ttgrid**) to locate the events. We define three ttgrid files for local, regional, and teleseismic distances. The local ttgrid file covers a radius of 8.0 degrees centered on the NISN network with grid spacing of 2.5 km between nodes. The regional ttgrid file extends to 20.0 degrees from NISN with grid spacing of 8.0 km. The output CSS3.0 database consists of *origin*, *event*, *arrival*, and *assoc* tables with NISN stations and KSIRS elements.

After the automatic processing is completed to produce the initial database, we attempt to associate arrival lists from IRSC and ISK networks in Iran and Turkey, respectively, to the origins. We then review both waveform and arrival data for each event in chronological order. Antelope program **dbloc2** is used to analyze events which includes reviewing phase picks on displayed waveforms such as retiming, renaming, adding, or deleting arrivals as required. After the analysis is finished, the event is relocated in **dbloc2** with **LocSAT** software using a 1D velocity model derived from previous studies in the region as shown in Table 1.

Table 1. 1D velocity model for the Middle East region

Depth (km)	P velocity (km/sec)	S velocity (km/sec)
0.0	2.50	1.10
1.0	4.00	2.10
9.0	6.00	3.50
19.0	6.40	3.60
39.0	7.10	3.90
50.0	8.00	4.52
210.0	8.30	4.70

We have completed processing of 11, 219 events recorded by the deployments and regional seismic networks in the Middle East from 2006 to 2010. Figure 5 shows distribution of the 11,219 seismic events along with 188 regional seismic stations that recorded the events. Among the 11,219 seismic events, 5,664 are with magnitudes above 2.0 with the greatest event at magnitude 6.5 (Figure 6). The depth distribution of the events is shown in Figure 7. Majority of the seismic events occurred at shallow depths of 40km or less. When relocating the seismic events, we fixed the depths at 15km if the relocation failed to converge or yielded abnormal uncertainties. Figure 8 represents statistics of semi-major axis of error ellipses for the relocated events. The maximum population occurs at 5km. 48% of the events have errors less than 10km, and 75% less than 20km. We perform quality control on the phase picks and abnormal arrivals are eliminated to ensure quality of the data. As the double-difference tomography software utilizes the first P and S arrivals only, we retain the Pg and Sg arrivals for epicentral distances less than the cross-over distance (set at 2.2° for the study area), and Pn and Sn for epicentral distances greater than the cross-over distance. Figure 9 shows 87,395 P and 69,144 S arrivals of the phase picks after quality control. We then reformat the phase picks in a format required by the double-difference tomography software for subsequent tomography study in the region.

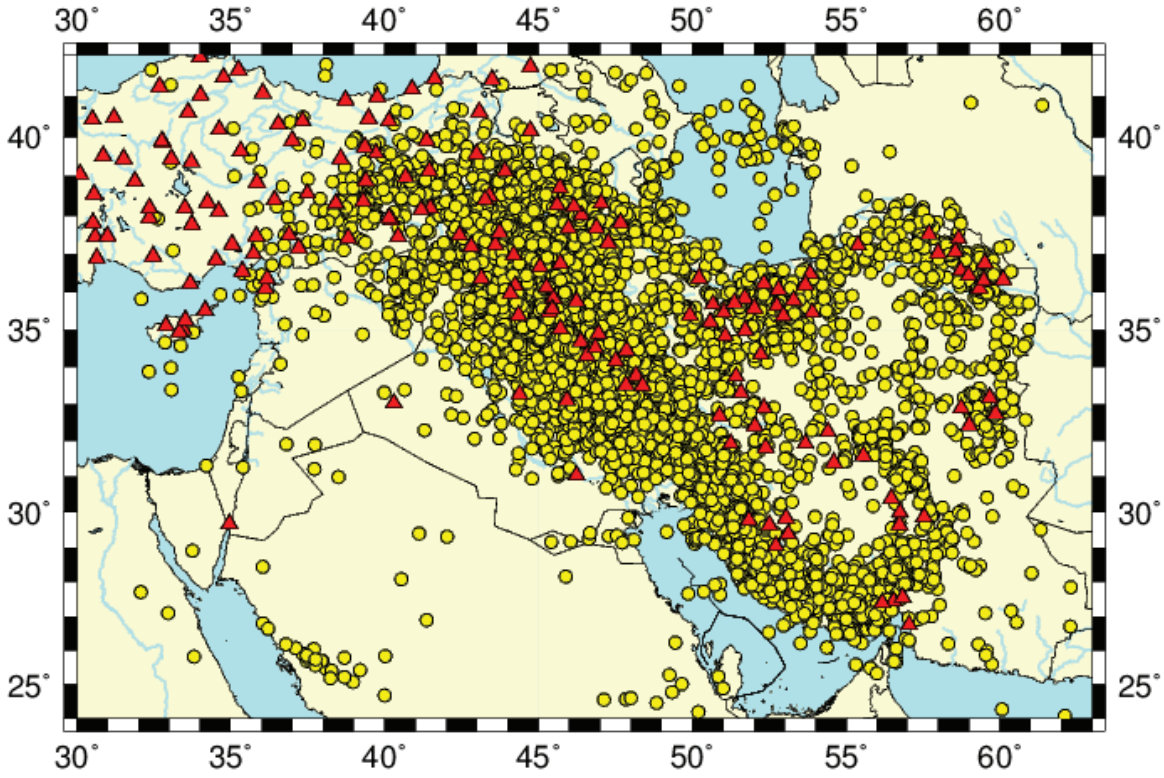

Figure 5. 11, 219 seismic events (yellow circles) recorded by 188 seismic stations (red triangles) from deployments and regional seismic networks in the Middle East from 2006 to 2010.

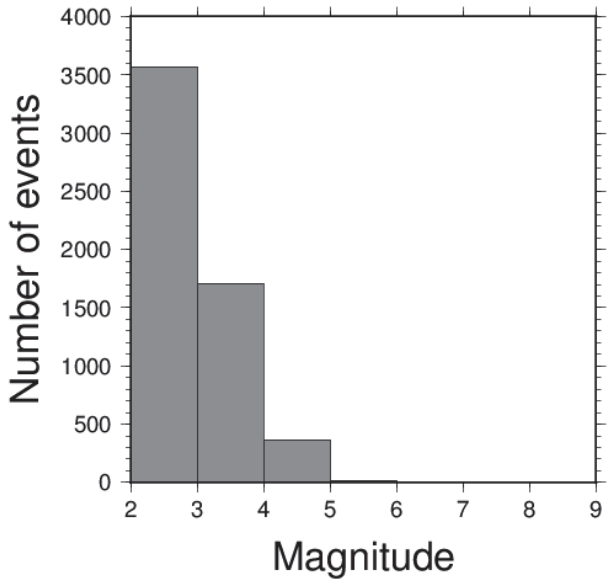

Figure 6. Magnitude distribution of the seismic events from 2006 to 2010 in the Middle East shown in Figure 5.

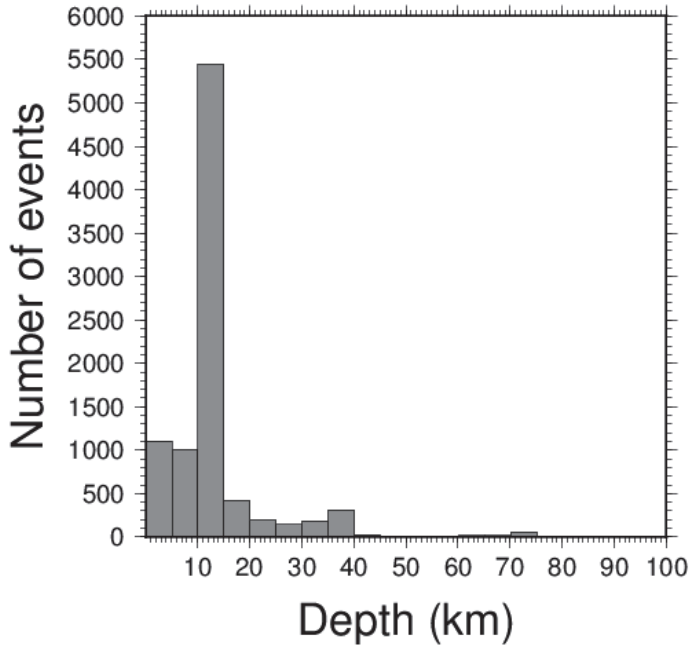

Figure 7. Depth distribution of the seismic events from 2006 to 2010 in the Middle East shown in Figure 5.

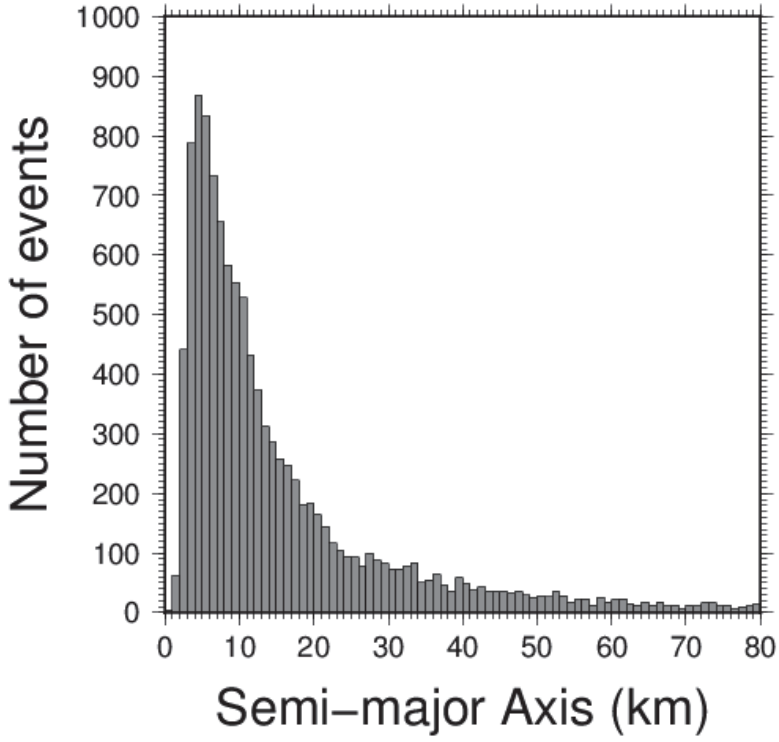

Figure 8. Statistics of semi-major axis of error ellipses for the processed seismic events in the Middle East from 2006 to 2010 shown in Figure 5.

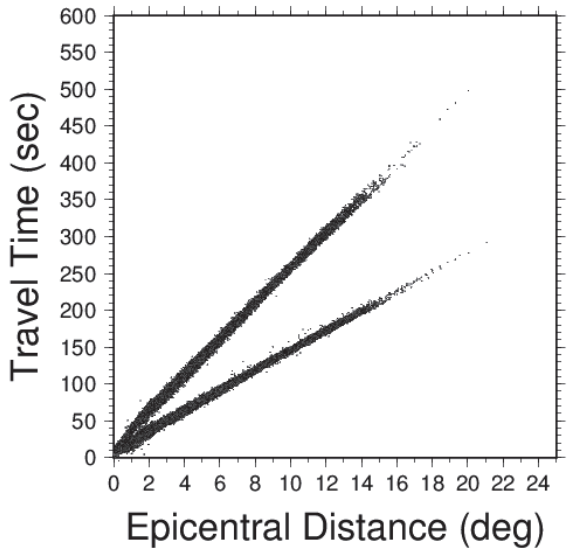

Figure 9. 87,395 first P and 69,144 first S arrivals after quality control for the seismic events recorded by deployments and regional seismic networks in the Middle East from 2006 to 2010 shown in Figure 5.

5.2. PROCESSING OF GCCEL BULLETIN DATA IN THE MIDDLE EAST

After we completed processing of the waveform and catalog data from 2006 to 2010 from the deployments and permanent regional seismic networks in the Middle East including the NISN, KSIRS, ISN networks in Iraq and other seismic networks from Iran and Turkey, we noticed that the events and stations have a dense coverage in the northeastern region of the study area, but the coverage in the southwestern region is rather sparse (Figure 5). We try to fill the gap and improve coverage of the study area by utilizing other available data in the region.

The Global Catalog of Calibrated Earthquake Locations (GCCEL) is repository of calibrated earthquake locations with phase picks. The event locations are determined using the Hypocentroidal Decomposition algorithm for multiple event relocation. The clusters of earthquakes are typically up to about 150 km in size and contain up to about 200 events. The location uncertainties including depth for the events are less than 5km. We retrieved 18 earthquake clusters from the GCCEL database in the Middle East including Ahel, Aligudarz, Avaj, Dorud, Fin and Tiab, Ghir, Kaki, Panjwin, Qom, Tabas from Iran, Dead Sea and Negev from Israel, Spitak from Armenia, Lank from Azerbaijan, Aqa from Saudi Arabia, Gazl from Uzbekistan, Racha from Georgia, and Tadjou from Djibouti. We examine phase picks from the data sets and retain the first P and S arrivals as our tomography will utilize the first arrivals only. Figure 10 illustrates seismic events in the Spitak cluster in Armenia and regional stations used for relocation of the events. There are 62 events in the cluster from 1961 to 2016. The magnitudes of the events range from 2.4 to 6.0, and the depths from 5.0 to 22.8km. Figure 11 represents ray path of the phase picks in the Spitak cluster. Figure 12a shows the travel times from all phase picks in the Spitak cluster, and Figure 12b the first P and S arrivals retained for subsequent tomography. Figures 13 and 14 illustrate 49 events in the Aqaba cluster in Saudi Arabia. We have processed a total of 1,620 seismic events recorded by 1,476 seismic stations in the GCCEL database in the region (Figure 15). The travel times of the P and S arrivals show little scattering, which indicates high quality of the phase picks (Figure 16). The ray paths from the GCCEL clusters provide additional coverage of the study

area, especially in the southwestern region where our original data from the Middle East lack coverage.

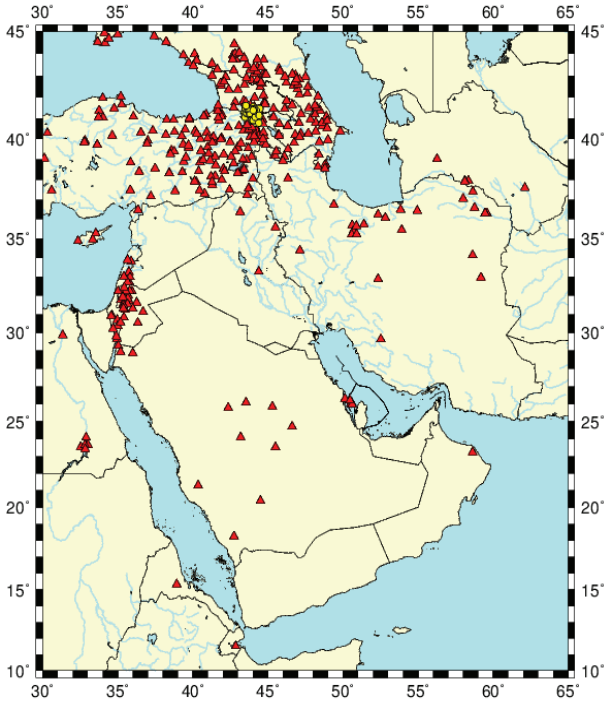

Figure 10. 62 seismic events (yellow circles) in the Spitak cluster in Armenia from the GCCEL with phase picks from seismic stations (red triangles) in the area.

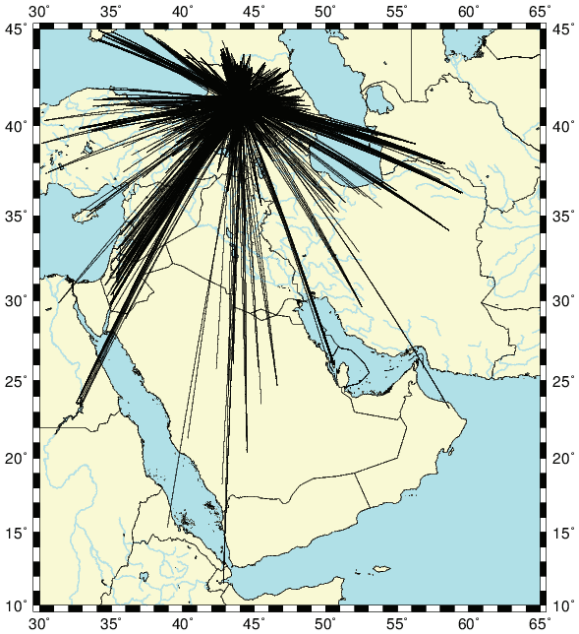

Figure 11. Ray path coverage from the seismic events in the Spitak cluster in the GCCEL shown in Figure 10.

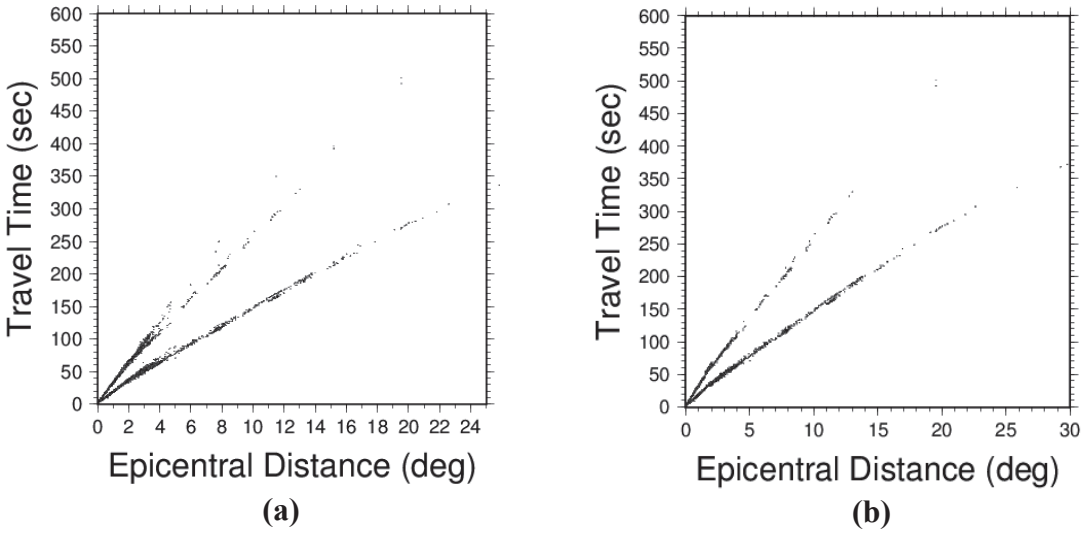

Figure 12. (a) travel times from all phase picks in the Spitak cluster in the GCCEL including Pg, Pn, P, Sg, Sn, S etc. (b) travel times of the first P and S arrivals retained for subsequent tomography.

Figure 13. 49 seismic events (yellow circles) in the Aqaba cluster in Saudi Arabia from the GCCEL with phase picks from seismic stations (red triangles) in the area.

Figure 14. Ray path coverage from the seismic events in the Aqaba cluster in the GCCEL shown in Figure 13.

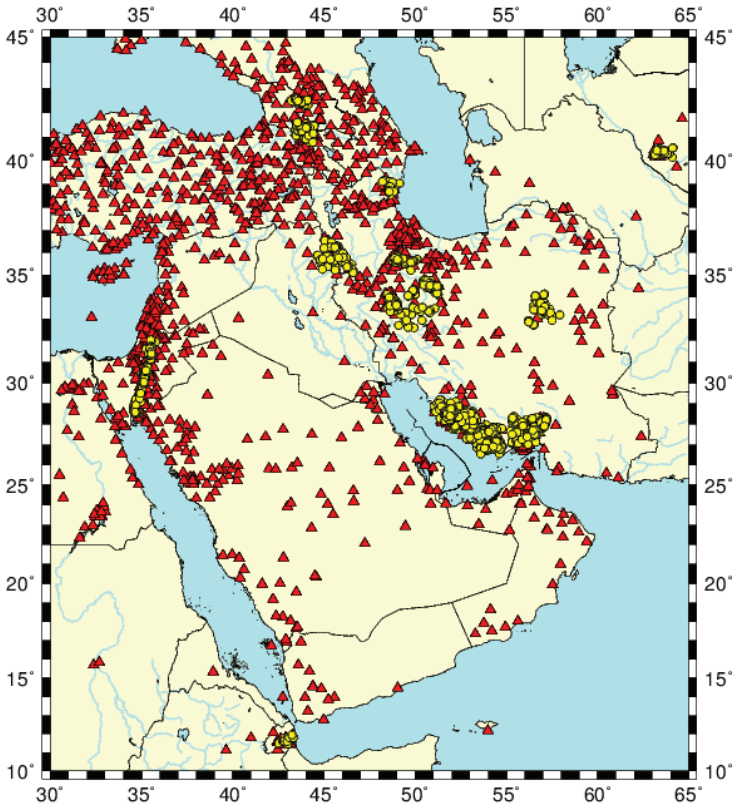

Figure 15. 1,620 seismic events (yellow circles) recorded by 1,476 seismic stations (red triangles) in the GCCEL database in the Middle East.

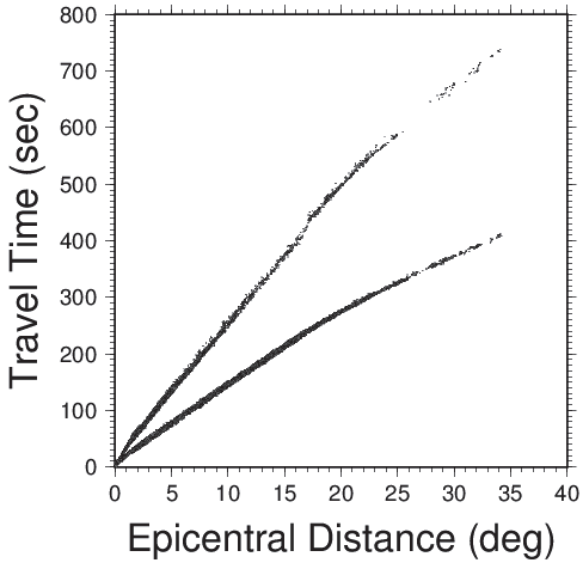

Figure 16. First P and S travel times from the events in the GCCEL database in the Middle East shown in Figure 15.

5.3. PROCESSING OF OTHER BULLETIN DATA IN THE MIDDLE EAST

As the seismic events in the GCCEL database are relocated in clusters, the events are not evenly distributed in the study area, resulting in less than ideal coverage of the study area (Figure 15). We try to improve coverage of the study area by including bulletin data from other seismic networks in the region. We retrieve bulletin data from the JSO network in Jordan from 2012 to 2016. There are 1,573 events recorded by 81 stations in the dataset. To ensure high-quality of the travel times, we only select phase picks with residuals less than 5 seconds and retain the first P and S arrivals. In processing the bulletin data from JSO, we found abnormal arrivals indicated as a secondary P arrival in Figure 17a. Further investigation into the original bulletins reveals that the secondary P arrivals are from deep earthquakes with depth greater than 300km. As previous studies indicate that there are few deep earthquakes in the region except along the Zagros fold and thrust belt, we suspect that these deep earthquakes have unreliable depths. We restrict event selection to those with depths less than 100km and perform quality control to eliminate the outliers. 1,433 events are retained after the quality control processing. The magnitudes of the processed events range from 0.0 to 7.2, and depths from 0 to 96km. The travel times of the first P and S arrivals after quality control are shown in Figure 17b that exhibit much improved data quality. Figures 18 and 19 show the distribution of the 1,433 events and ray path coverage of the phase picks, respectively. The dataset provides additional coverage in the southwestern region, which will improve the resolution of subsequent tomography in the area.

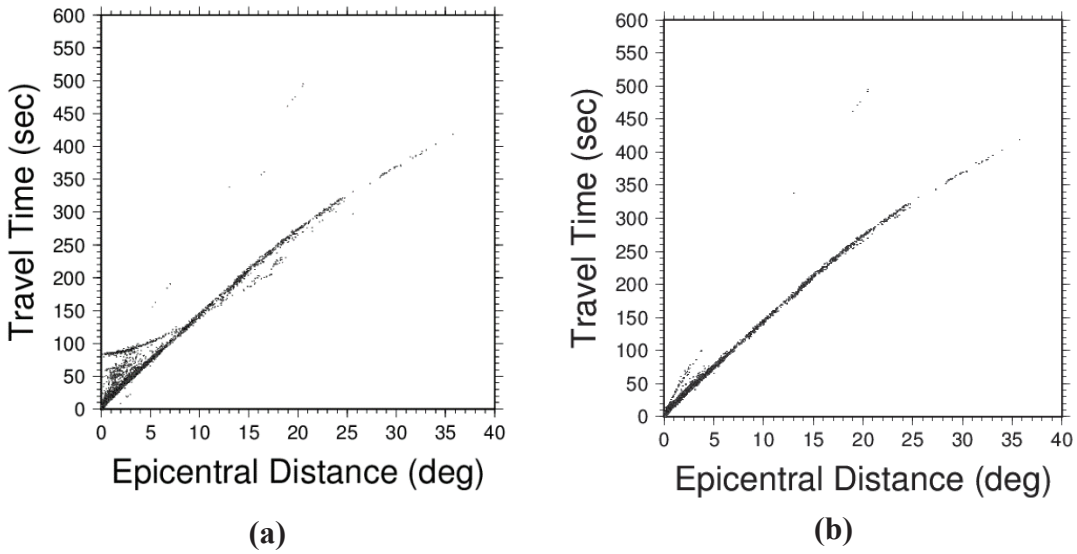

Figure 17. (a) travel times of the first P and S arrivals from all events in the JSO bulletins from 2012 to 2016. (b) travel times of the first P and S arrivals from retained events after quality control.

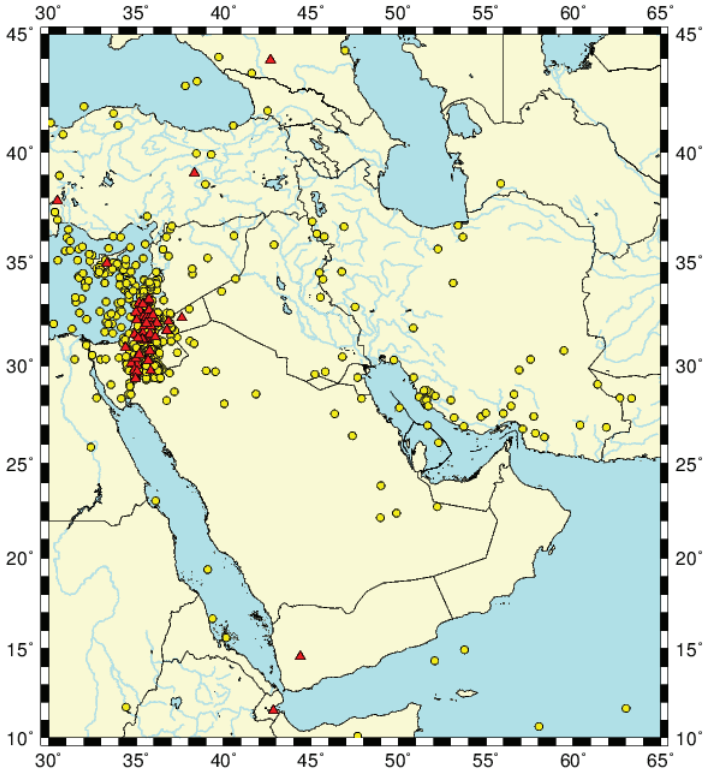

Figure 18. 1,433 seismic events (yellow circles) from 2012 to 2016 recorded by the JSO network (red triangles) in Jordan.

Figure 19. Ray path coverage of the seismic events recorded by the JSO network shown in Figure 18.

To further improve coverage of the study area, we also collected and processed seismic data from other regional seismic networks in the Middle East including those from Israel, Saudi Arabia, Syria, UAE, Oman, and Yemen. We restrict the selection of events and stations in an area with latitudes from 10ºN to 45ºN, and longitudes from 30ºE to 65ºE. The depth is limited to 100km or shallower. To ensure reliability of event locations, we select the events in the bulletins recorded by at least five stations. Only the phase picks with travel time residuals less than 5 seconds are retained to assure quality of the data. We processed 18,869 events from 1985 to 2018 from the networks in Israel, 20,168 events from 2001 to 2017 from Saudi Arabia, 6,967 events from 2002 to 2013 from Syria, 2,759 events from 2010 to 2016 from UAE, 4,440 events from 2003 to 2016 from Oman, and 2,205 events from 2000 to 2012 from Yemen. Figure 20 shows the distribution of seismic events recorded by the Saudi Arabian networks. Figure 21 represents the first P and S phase travel times from the dataset after quality control. Figures 22 illustrates the distribution of the events recorded by the Oman networks, and Figure 23 indicates the first P and S phase travel times from the dataset after quality control.

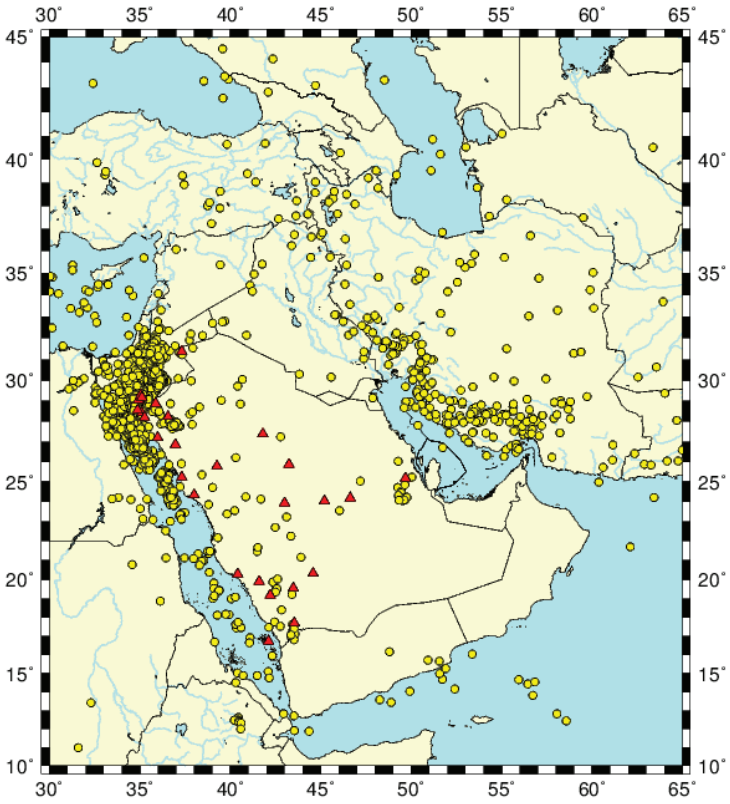

Figure 20. Seismic events (yellow circles) recorded by seismic stations (red triangles) in the Saudi Arabian networks.

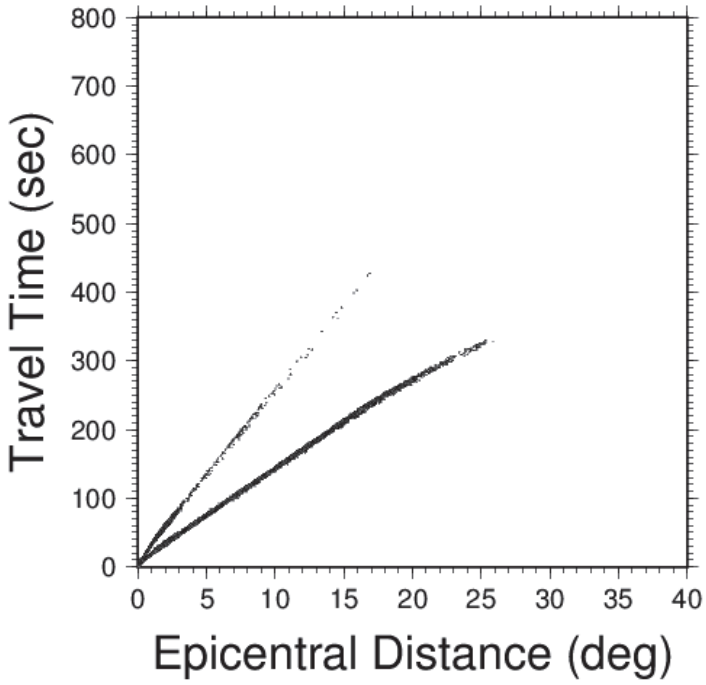

Figure 21. First P and S travel times from the events recorded by the Saudi Arabian networks shown in Figure 20.

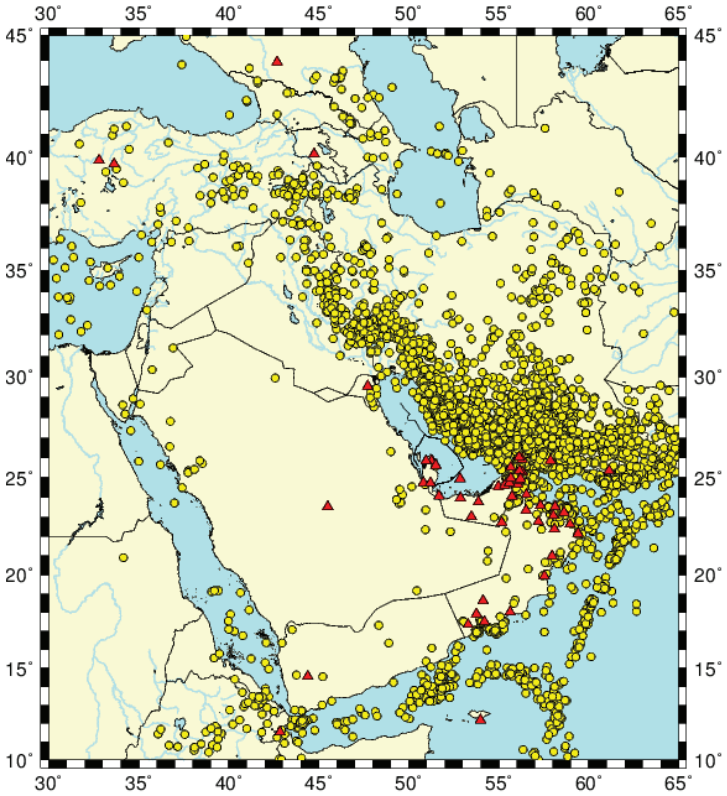

Figure 22. Seismic events (yellow circles) recorded by seismic stations (red triangles) in the Oman networks.

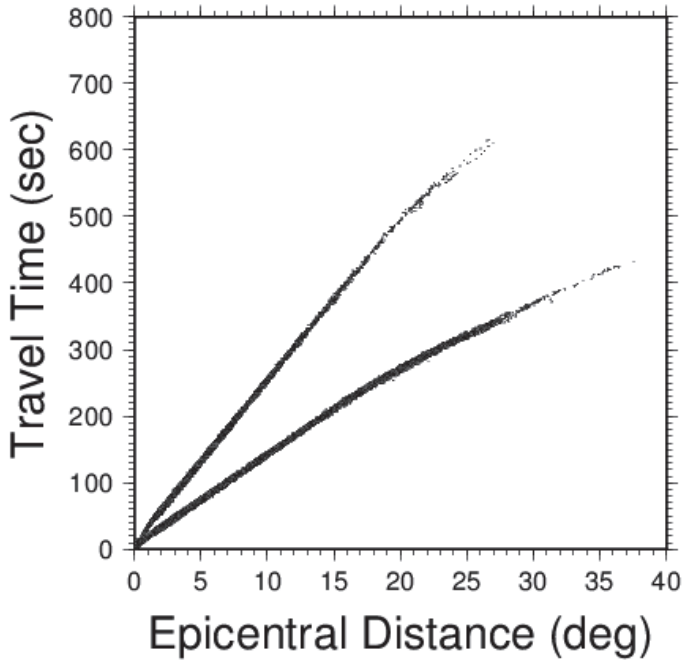

Figure 23. First P and S travel times from the events recorded by the Oman networks shown in Figure 22.

5.4. PROCESSING OF AMBIENT NOISE DATA IN THE MIDDLE EAST

We collected continuous recordings from the NISN, KSIRS and ISN networks from 2009 to 2010. The original waveforms are in hourly segments. We attempt to merge the hourly segments into daily traces. The hourly segments are read in the SAC program and the SAC command "merge" is used to merge them into a single 24-hour trace. When performing the merge, we find that some of the resultant daily traces have unexpected spikes that are not in the original hourly data. An example of merged trace with wrongful spikes is shown in Figure 24. After some debugging, we discover that the unexpected spikes are the result of the limited precision of internal time in the SAC software. Because of the limited precision in the internal time in SAC, there is a small discrepancy between the actual time of the recordings and the time represented in the SAC software. The small discrepancies in the time in SAC accumulate as the merge process proceeds. Eventually a gap appears between the segments, and a spike is generated as the segments are merged in SAC. To avoid this pitfall, we read the last hourly segment first in SAC, and read the previous hourly segment and merge them. The previous hourly segment before the merged segment is then read in and merged with current one, and so on. In this procedure, the starting time of the merged segments are reset every time a new segment is merged in, and the discrepancy in time never grows large enough to generate a gap in time. Figure 25 shows the merged daily recording following the new procedure for the same data shown in Figure 24, and the unexpected spikes are no longer existent. We also manually examine each merged daily trace and eliminate those with glitches such as spikes and gaps and malfunctioning of the instruments. Figure 26 shows an example of abnormal recordings that have been discarded in the check, and Figure 27 represents a 24-hour continuous trace that is kept after the merge and quality control.

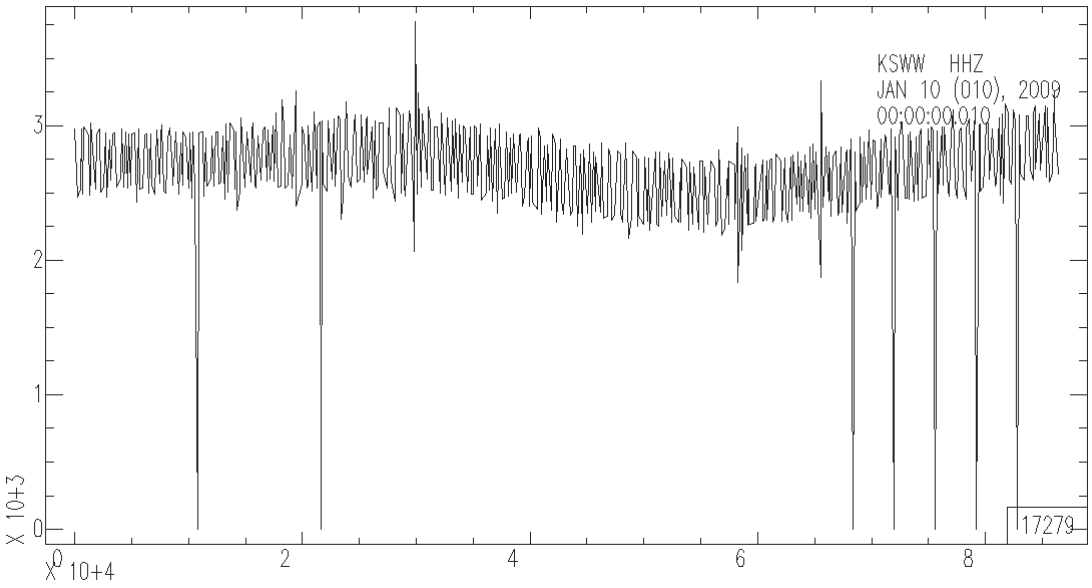

Figure 24. 24 hourly segments on January 10, 2009 from the NISN station KSWW are read in SAC and merged using the "merge" command. *Unexpected spikes not in the original hourly segments are present after the merge.*

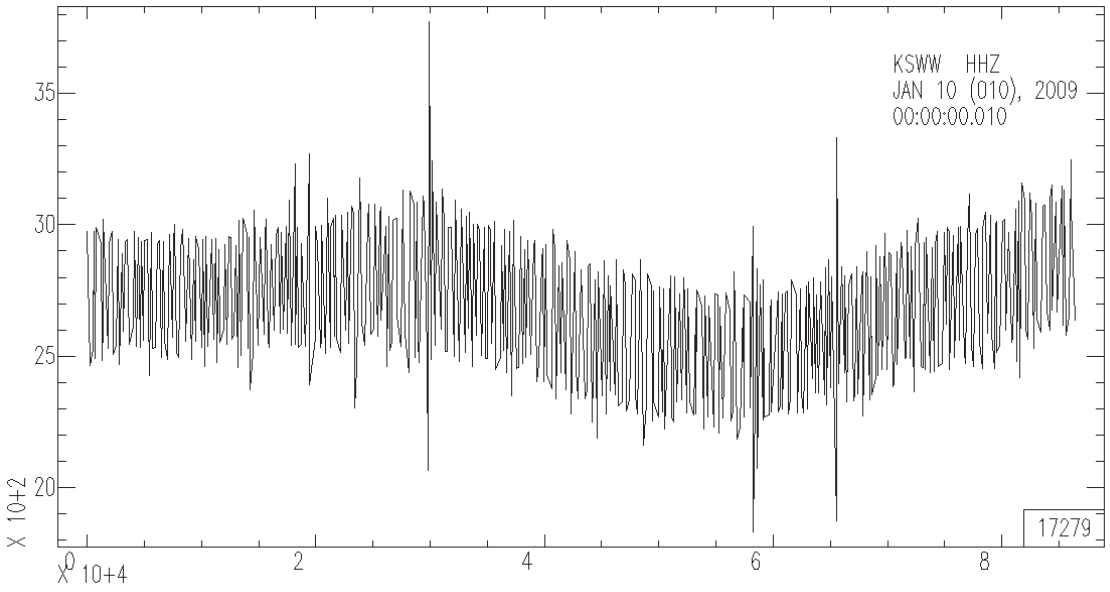

Figure 25. Merged 24-hour recording on January 10, 2009 from the NISN station KSWW following the new processing procedure described in the report. *The unexpected spikes shown in Figure 24 are eliminated.*

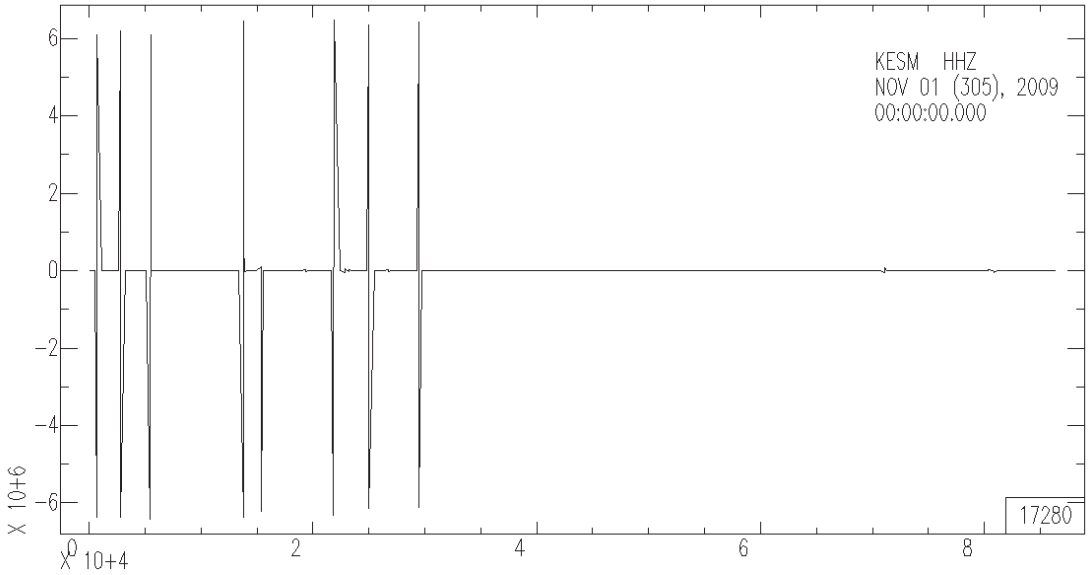

Figure 26. Waveform recorded by the NISN station KESM on November 1, 2009. *Multiple glitches exist in the recording, and the trace is discarded to ensure quality of the ambient noise data.*

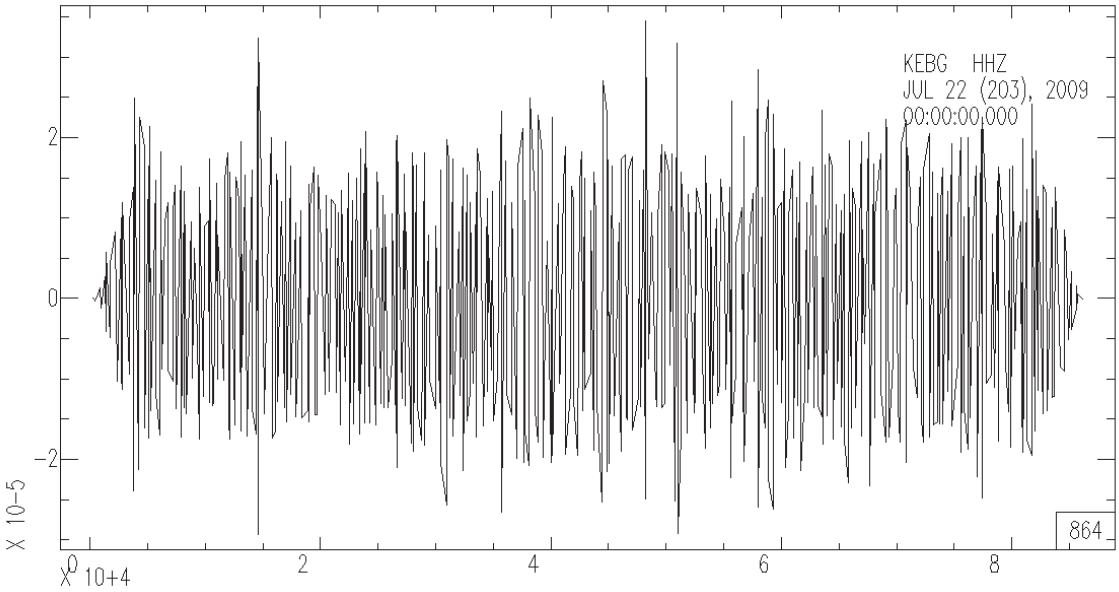

Figure 27. 24-hour continuous trace of vertical recording from the NISN station KEBG on July 22, 2009 after merge and quality control.

Ambient noise carries information about the Earth media, and it is demonstrated that ambient-noise cross-correlation can be used to retrieve surface wave Green's functions between station pairs [19]. The obtained surface wave Green's functions can then be utilized to invert for 3D Earth structures [6]. Processing of ambient noise data for extraction of surface wave dispersion consists of several steps including single station data preparation, cross-correlation and temporal stacking, and measurement of dispersion curves [31].

The first step of ambient noise processing involves preparation of single station recordings. The purpose is to remove earthquake signals and instrumental irregularities that tend to obscure ambient noise. We first remove the instrument responses from the recordings, then de-mean, de-trend, and band-pass filter the seismograms in the frequency band from 1s to 100s. The seismograms are then resampled to 5sps to reduce computational load in the cross-correlation calculation. Temporal normalization and spectral whitening using a running window approach are then performed to suppress the earthquake and other contaminating signals. Multiple frequency bands in 2-5s, 5-10s, 10-20s and 20-40s are used for temporal normalization. We stack the normalized traces to form one single broadband wave train, and then perform cross-correlation. This aims to achieve more even energy distribution in both the time and frequency domain. The cross-correlation of daily recordings of station pairs are then stacked to yield the final cross-correlation functions.

We processed ambient noise recordings from the stations in the NISN, KSIRS and ISN networks in 2009 and 2010. Figure 28 shows the stacked cross-correlation functions between the station pairs. Surface wave signals are clearly observed between group velocities 2km/s to 4km/s.

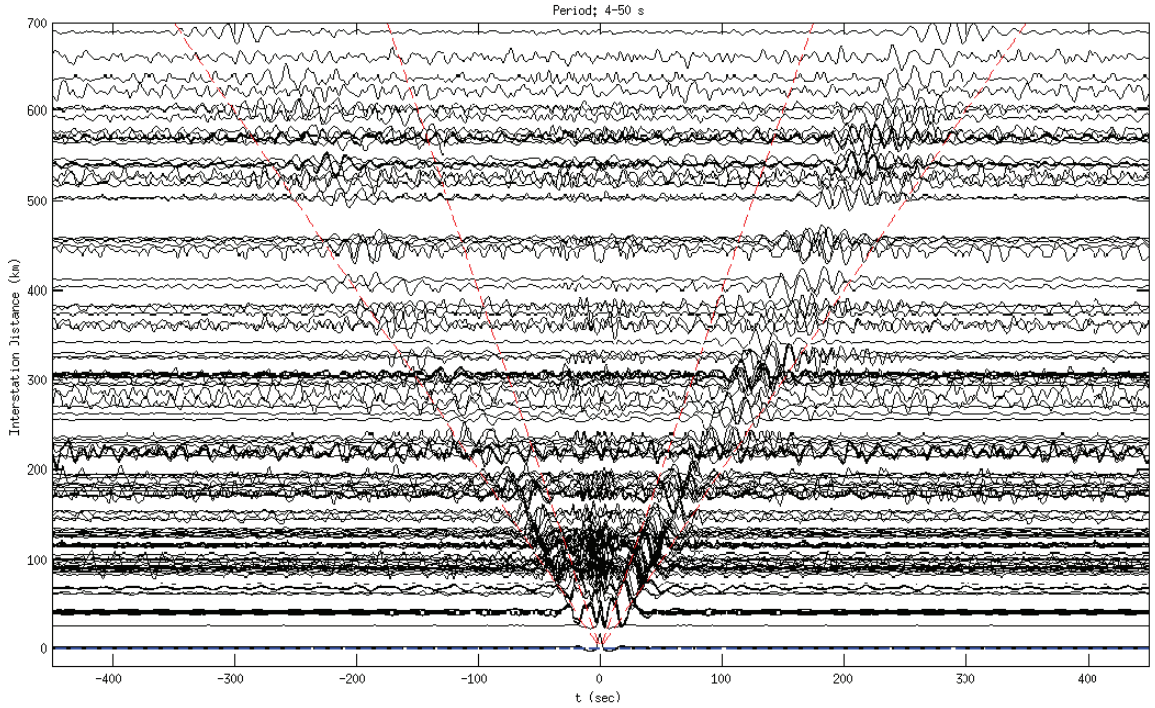

Figure 28. Cross-correlation functions obtained from stacking of cross-correlation of daily ambient noise data recorded in 2009 and 2010 by seismic stations in the NISN, KSIRS, and ISN networks in the Middle East. *The x-axis denotes time (second), and the y-axis the inter-station distance (km). The two red dashed lines represent group velocities at 2km/sec and 4km/sec, respectively.*

We adopt the EGFAnalysisTimeFreq dispersion software to measure surface wave dispersion between the station pairs [32]. This Matlab GUI software is used for extracting group and phase velocity dispersion curves from surface wave empirical Green's functions (EGF) or cross-correlation functions (CF) from ambient noise. The dispersion analysis is based an imaging analysis technique [32-34], which automatically traces the dispersion curve on the phase or group velocity-period image. We select the surface wave signals on the CF in a group velocity window between 1.0km/sec and 5.5km/sec. A noise window of 150sec long is chosen right after the signal window. A signal-to-noise ratio (SNR) threshold of 5 is adopted. Figure 29 shows an example of the CF and SNRs for the station pair of IBDR and KSJS. Figures 30 and 31 illustrate extraction of Rayleigh wave group and phase velocities on the CF between IBDR and KSJS. We obtained phase and group velocity measurements from 121 pairs of seismic stations in the Middle East. The path coverage of the measurements is shown in Figure 32.

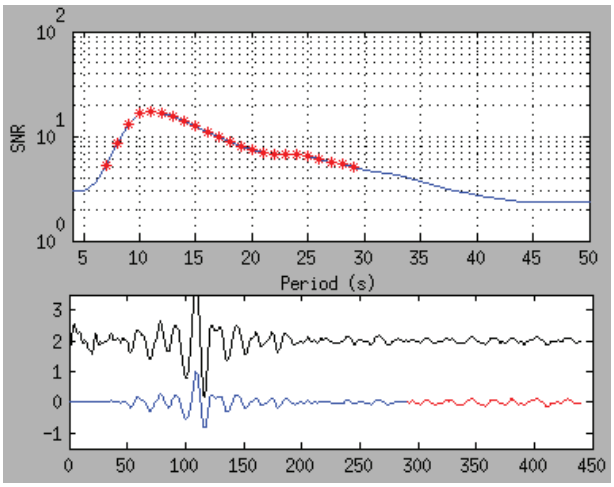

Figure 29. (Top) SNRs for the CF of station pairs of IBDR and KSJS. The red stars indicate those above the threshold of 5. (Bottom) The top black trace is the stack of the positive and negative time CF (the so-called symmetric component). *The bottom blue part of the trace shows the signal (within group velocity windows between 1.0km/sec and 5.5km/sec) and the red part for noise (150s long, right after the signal window).*

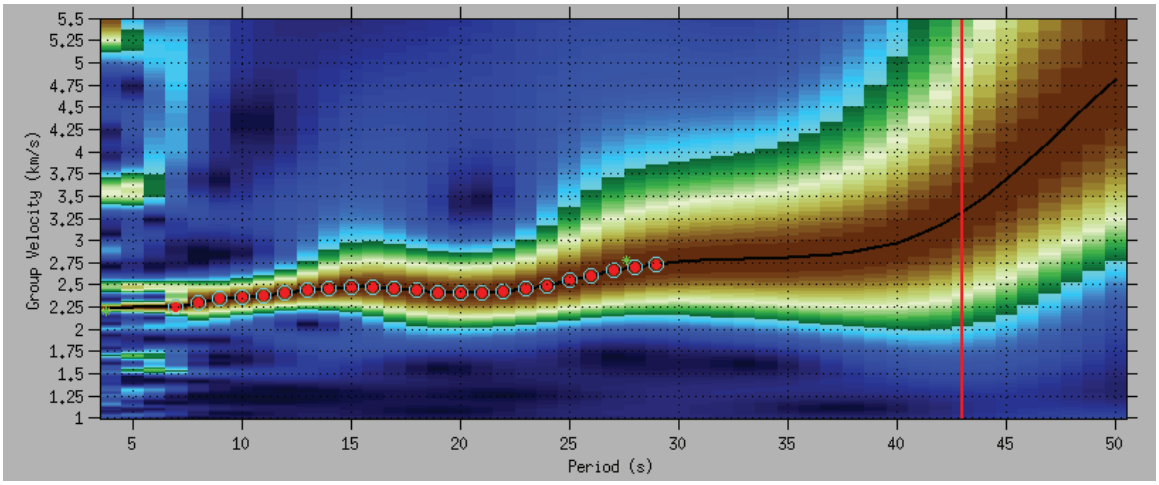

Figure 30. Group velocity dispersion analysis on the CF of station pair IBDR and KSJS. Horizontal axis denotes period (s), and vertical axis group velocity (km/s). *The black curve represents the traced dispersion curve with the light blue open circles for periods above the SNR threshold of 5 and red solid circles for the periods saved for group velocity dispersion. The vertical red line indicates the period at which the inter-station distance is twice the wavelength.*

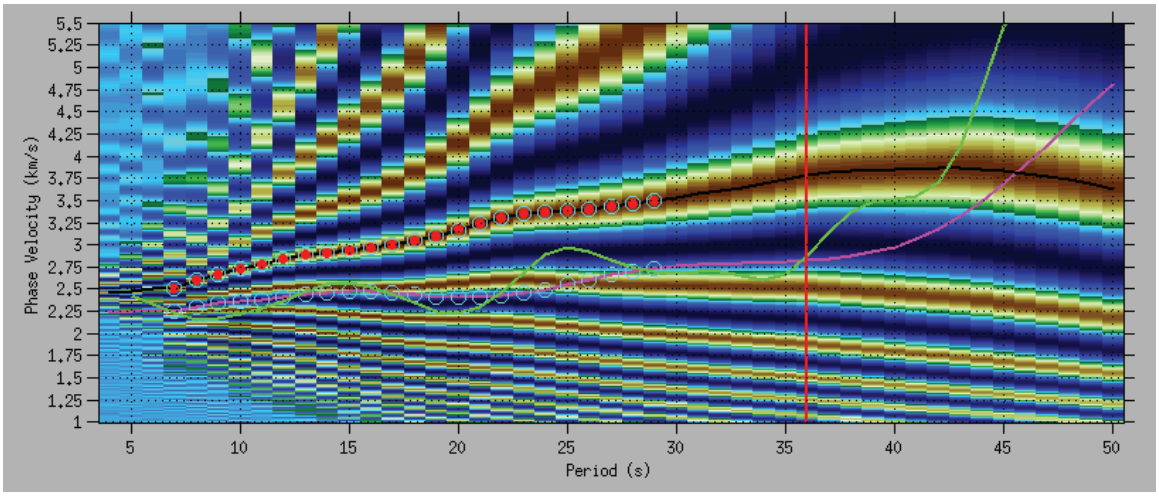

Figure 31. Phase velocity dispersion analysis on the CF of stations IBDR and KSJS. *Horizontal axis denotes period(s), and vertical axis phase velocity (km/s). The black curve represents the traced dispersion curve with the light blue open circles for periods above the SNR threshold of 5, and red solid circles for the periods saved for phase velocity dispersion. The vertical red line indicates the period at which the inter-station distance is twice the wavelength. The group dispersion curve traced previously (Figure 30) is shown in magenta and the points that have been picked are plotted as cyan circles. The group velocity dispersion can be used as a reference for phase velocity dispersion pick. We also compute the group velocity dispersion curve from the picked phase velocity dispersion using the formula g = c + k*dc/dk, where g and c are the group and phase velocities, respectively, and k is the wave number, shown as the green line to compare with the picked group velocity dispersion.*

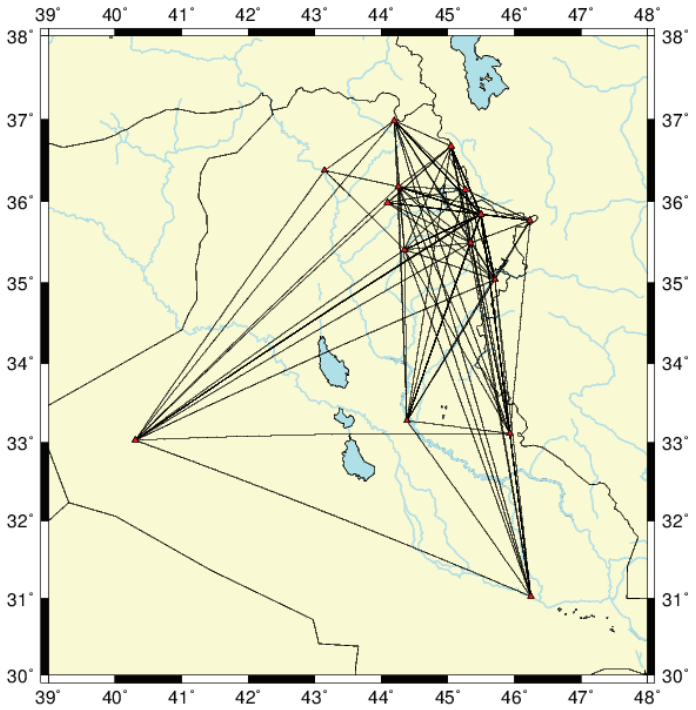

Figure 32. Path coverage of 121 pairs of seismic stations for which surface wave dispersion measurements are obtained.

5.5. MEASURING SURFACE WAVE DISPERSION FROM EARTHQUAKES IN THE MIDDLE EAST

As continuous seismic recordings are only available for a limited number of stations in the study area for extraction of surface wave dispersion, we also utilize seismic data of earthquakes recorded by the stations in the Middle East to measure surface wave dispersion between earthquakes and stations. The waveforms in SEED format are extracted and stored in SAC format. Figure 33 shows the vertical recordings of an M5.1 event that occurred at 20:06:37.34 UTC on March 11, 2002 at latitude 25.148°N and longitude 56.068°E. The pole and zero responses are also extracted from the SEED volumes and utilized to correct for instrument response. The waveforms are cut in a time window defined by group velocities 2 and 5 km/sec and decimated from 100 sample per second to 20 sample per second. We then remove the linear trends from the data by using the SAC command *rtr* and reduce the original waveforms in velocity to ground motion in displacement by removing the instrument response using the SAC command *transfer*. In removing the instrument response, we use band pass frequency limits of 0.008 0.01 1.0 1.2 to prevent emphasizing low and high frequency noise.

We use a frequency-time analysis method based on the multiple filter technique (MFT) included in the **Computer Programs in Seismology** package by Robert Herrmann to process the regional waveforms. The MFT technique requires that the instrument response is removed, and the recordings are reduced to ground motion in displacement, velocity or acceleration in some frequency band. Specifically, the procedure includes making instrument response corrections, performing band-pass filtering of multiple bandwidths, calculating energy distribution in the time-frequency domain, picking out the energy peaks and a few local maxima at each period. Figures 34 and 35 represent screenshots of the MFT measurements of the event on March 11, 2002 shown in Figure 33 recorded at station ABKT and ISP, respectively. We processed seismic recordings from 256 events from 2001 to 2009 and obtained 2,988 Rayleigh wave group velocity dispersion curves. Figure 36 shows ray path coverage of the obtained Rayleigh wave dispersion data. We also performed quality control on the dispersion data by eliminating abnormal readings. Figure 37 represents the dispersion curves after quality control.

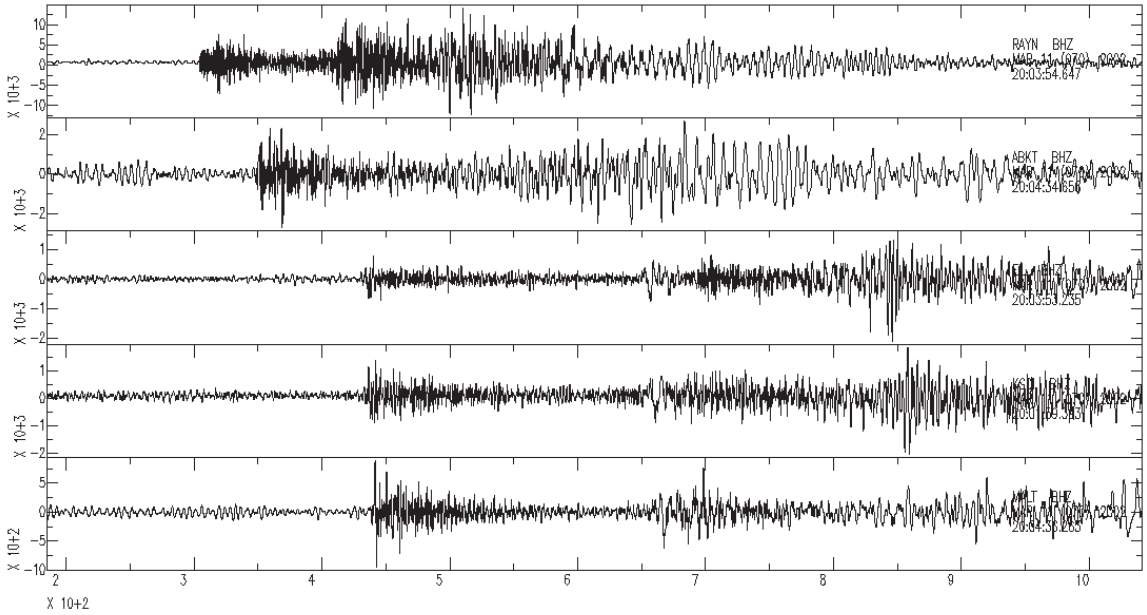

Figure 33. Vertical recordings of an M5.1 event that occurred at 20:06:37.34 UTC on March 11, 2002 at latitude 25.148°N and longitude 56.068°E in the Middle East.

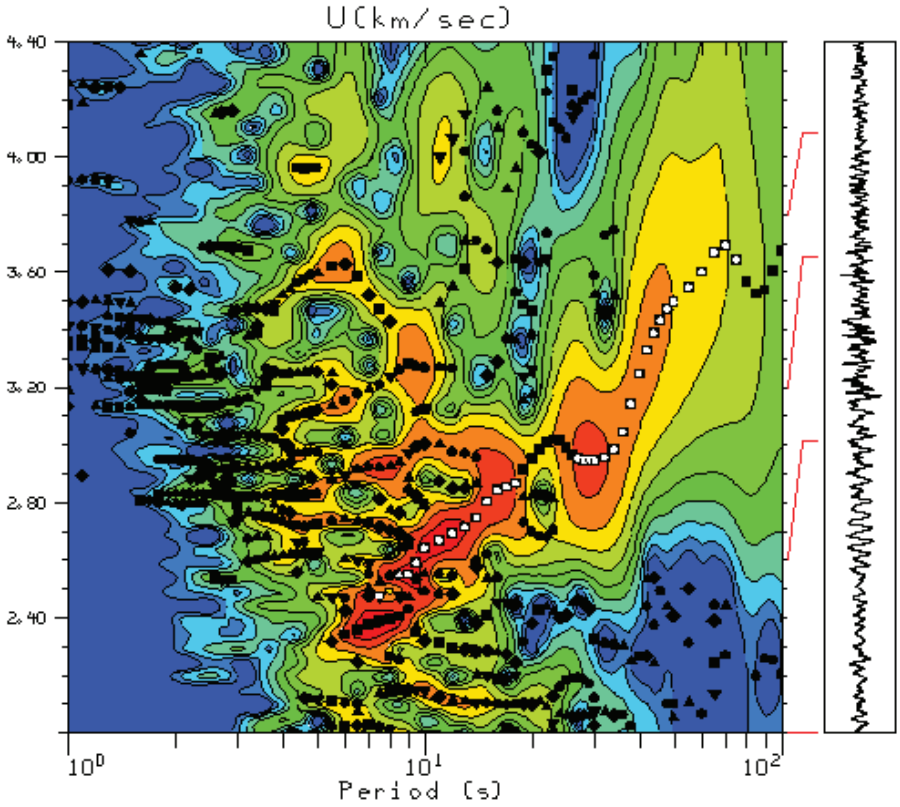

Figure 34. Screenshot of MFT processing of the event shown in Figure 33 at station ABKT at an epicentral distance of 1420 km.

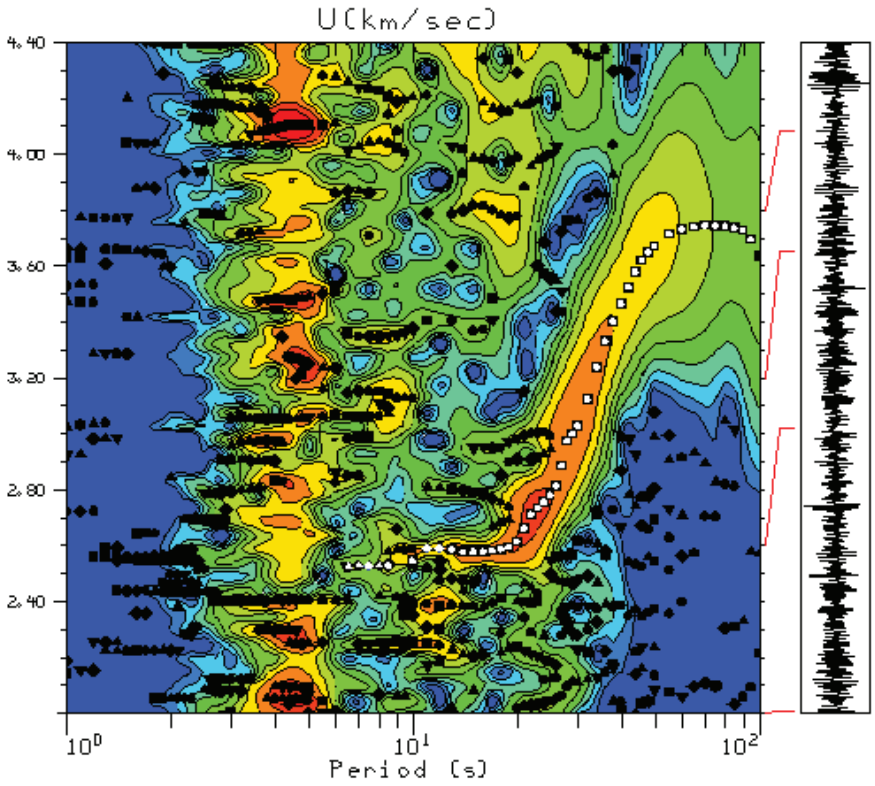

Figure 35. Screenshot of MFT processing of the event shown in Figure 33 at station ISP at an epicentral distance of 2793 km.

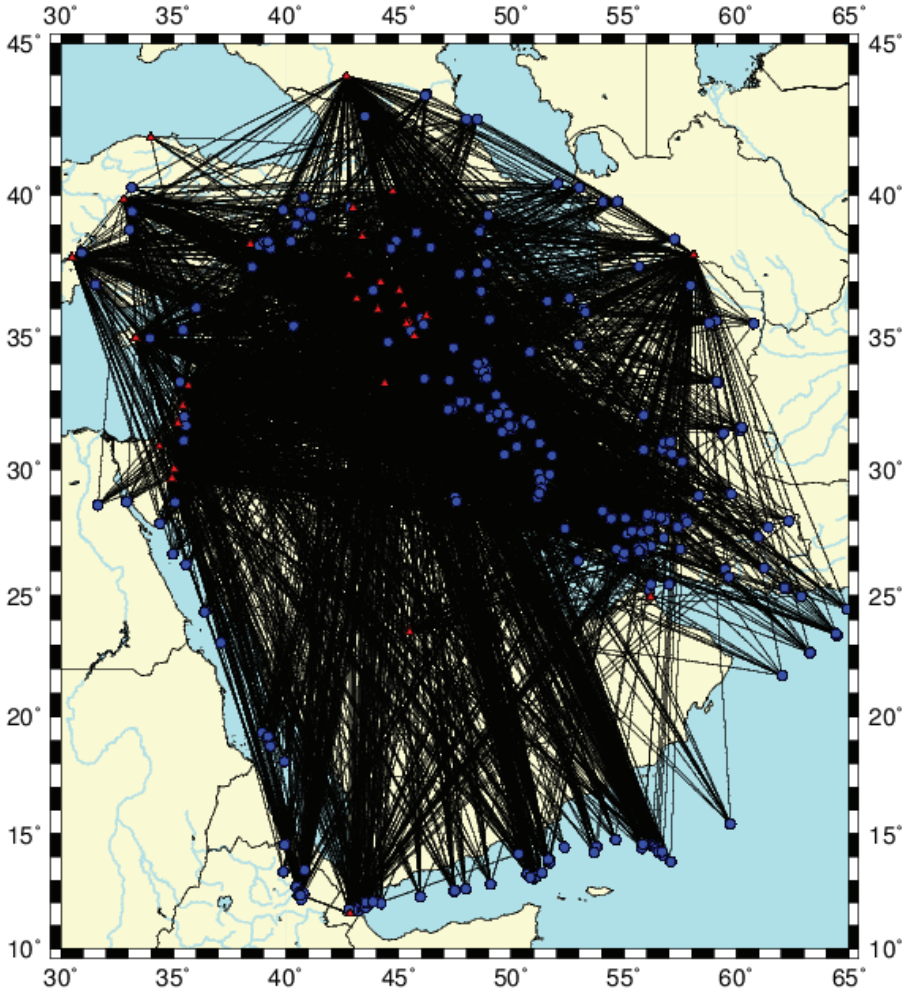

Figure 36. Ray path coverage of Rayleigh wave group velocity dispersion measurements in the Middle East. *The red triangles represent the seismic stations, and the blue circles the seismic events.*

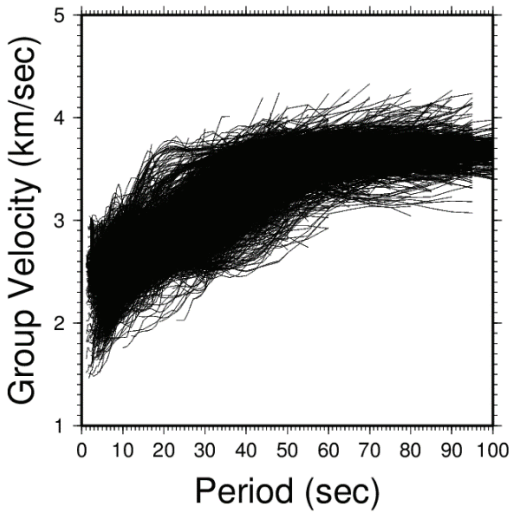

Figure 37. Rayleigh wave group velocity dispersion measurements from 2001 to 2009 in the Middle East.

5.6. PROCESSING OF RECEIVER FUNCTIONS IN THE MIDDLE EAST

We collected waveforms of teleseismic events recorded by seismic stations in the networks of NISN, KSIRS and ISN at epicentral distances from 30° to 90°. Teleseismic waveforms at additional seismic stations in the study area from latitudes 10ºN to 45ºN, and longitudes 30ºE to 65ºE are also collected from the IRIS, GFZ and ORFEUS data centers to improve coverage of the study area. There are a total of 42 seismic stations for which teleseismic waveforms are collected for receiver function analysis. Pre-processing of the waveforms are performed on the collected data. We first remove the instrument responses using the SAC command "transfer". The 3-componet recordings are then rotated to the vertical, radial and transverse directions. Receiver functions are finally calculated by time domain iterative deconvolution technique [26] with Gaussian widths of 1.0 and 2.5. Figure 38 illustrates teleseismic events recorded at station KIV that are utilized for the receiver function analysis. Figure 39 represents receiver functions with Gaussian width of 1.0 obtained at station KIV. As P waves from different distances have different incident angles which affects both the time and amplitude of the receiver functions, we correct the receiver functions to a reference slowness of 0.06 deg/s. We then remove the variations due to azimuthal dependence using the "harmonic stripping" technique [35] and stack the receiver functions at each station. Figure 40 illustrates the stacked receiver function with a Gaussian width of 1.0 at station KIV. We perform quality control on the receiver functions, and the abnormal ones and those with low quality are discarded to prevent contamination of the subsequent joint tomography results. Figure 41 shows the location of 25 stations for which the stacked receiver functions are kept after quality control and will be utilized in joint inversion with body wave travel times and surface wave dispersions for P and S velocity models for the Middle East.

Figure 38. Teleseismic events (red circles) recorded at station KIV (blue triangle) are utilized for receiver function analysis for the station. *The three black circles indicate epicentral distances of 30, 60 and 90 degrees, respectively.*

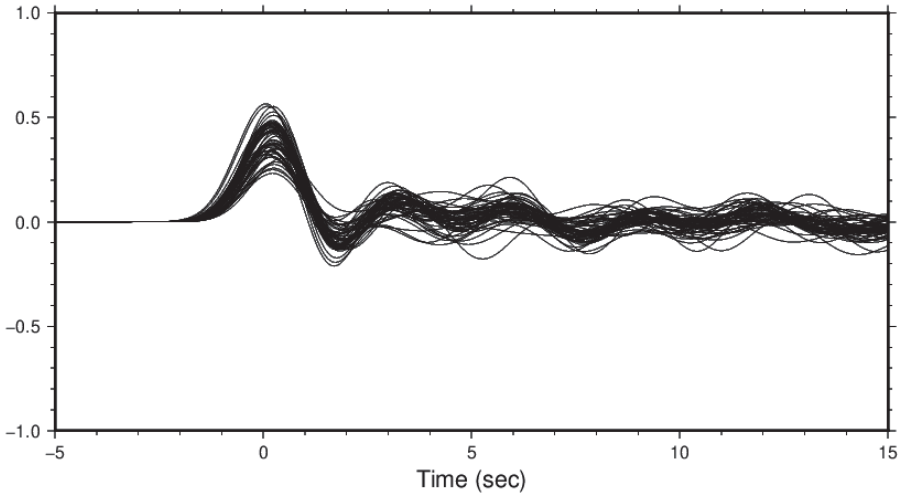

Figure 39. Receiver functions with a Gaussian width of 1.0 obtained at station KIV.

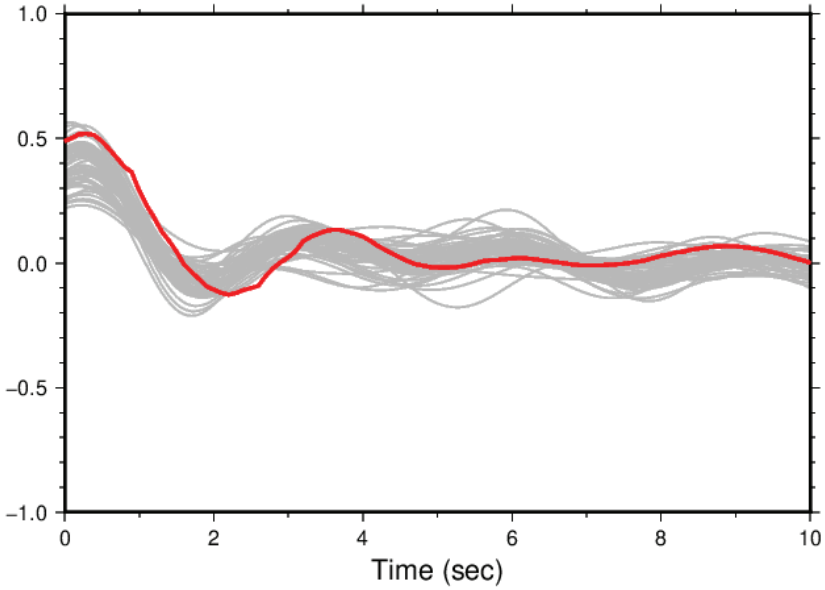

Figure 40. Stacked receiver function (red line) at a reference slowness of 0.06 deg/s at station KIV after distance and azimuthal corrections. *The original receiver functions used in the stacking are represented by the grey lines.*

Figure 41. Receiver functions are obtained at 25 stations (red triangles) in the Middle East.

5.7. JOINT TOMOGRAPHIC INVERSION FOR P AND S VELOCITY MODELS IN THE MIDDLE EAST

We conducted a joint inversion of body wave travel times, surface wave dispersion and receiver functions for high-resolution P and S velocity models of the Middle East. We utilize absolute body wave travel times, differential body wave travel times, surface wave dispersion between station pairs from ambient noise cross-correlation, surface wave dispersion between station and event pairs from earthquakes, and receiver functions. These data types complement and enhance each other and provide more complete and stricter constraints on the obtained velocity models. The absolute body wave travel times constitute the fundamental framework for the velocity models while the differential body wave travel times enhance the imaging in areas with a high-density of seismicity. The surface wave dispersion from earthquakes improves the model at shallow depths filling the gap of body waves due to sparse crossing rays of body waves near the surface. The surface wave dispersion from ambient noise further improves the coverage in seismically less active areas. The receiver functions provide better constraint on the velocity contrasts than the body and surface wave travel times. By combining the five data types, we expect to obtain more robust and reliable P and S velocity models for the region.

The study area is set in a region from latitudes 10ºN to 45ºN, and longitudes 30ºE to 65ºE. We divide the study area into 0.5ºx0.5º cells horizontally. In the vertical direction, we set up layers at 5km intervals from the Earth surface to the depth of 60km, and additional layers at 80, 120 and 210km. A 1D starting model is constructed based on a previous study of Pasyanos et al. (2004)

[36] for the crust and the AK135 model for the upper mantle. Figure 42 illustrates the 1D starting model of P and S wave velocities. We select 12,437 events recorded by 1,647 stations from the phase picks database that we have constructed for the region. Selection of the events is based on the density of event distribution in the region. For areas with high event density such as the Zagros fold belt, we select events recorded by at least 8 stations while for other areas, events recorded by 5 stations or more are selected to ensure adequate coverage of the study area. Figures 43 and 44 show horizontal and vertical distribution of the events adopted for the tomography, respectively. Figure 45 illustrates ray path coverage of the study area, and Figure 46 represents P and S travel times from the phase picks utilized in the tomography. The body wave data include 178,633 first P arrivals, 70,505 first S arrivals, 100,513 differential P arrivals, and 42,519 differential S arrivals.

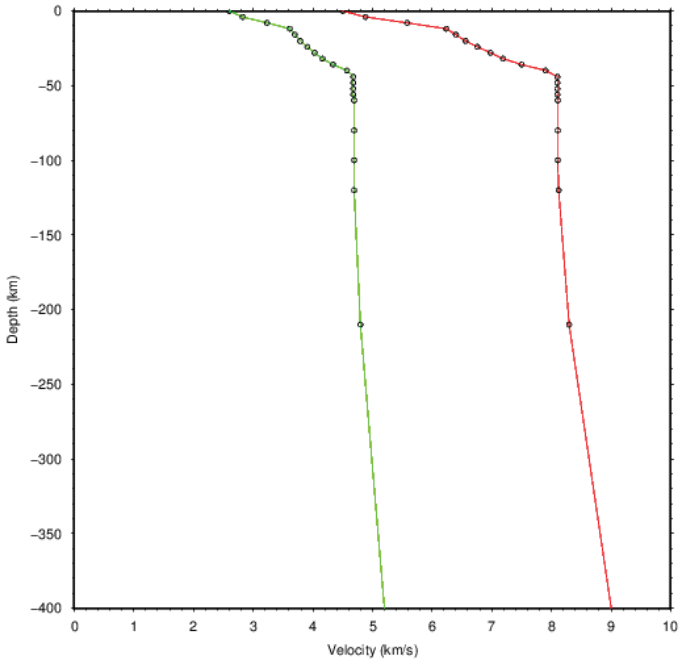

Figure 42. 1D starting models of P (red) and S (green) wave velocities adopted in the tomographic inversion.

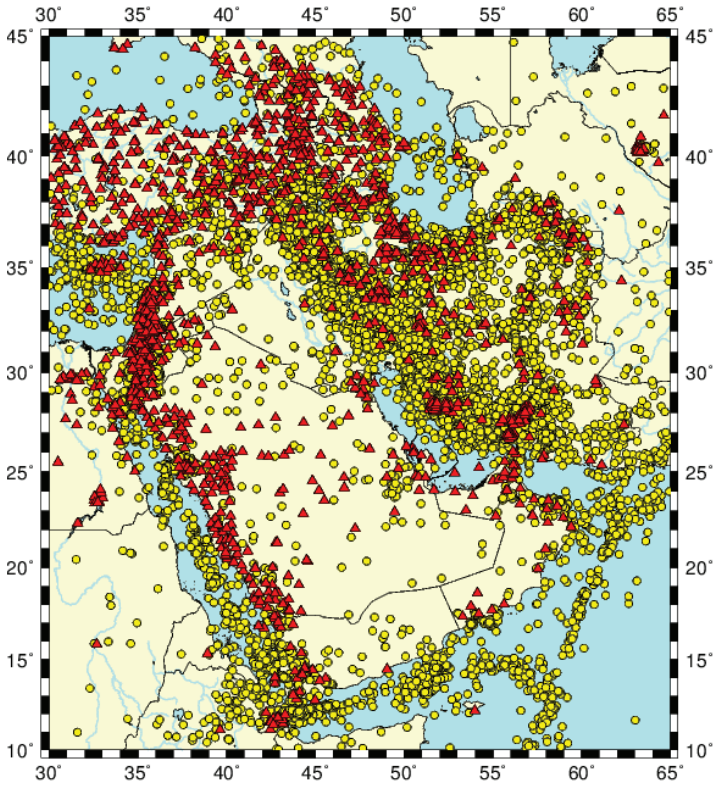

Figure 43. 12,437 seismic events (yellow circles) selected for the tomography and 1,647 stations (red triangles) that recorded the events.

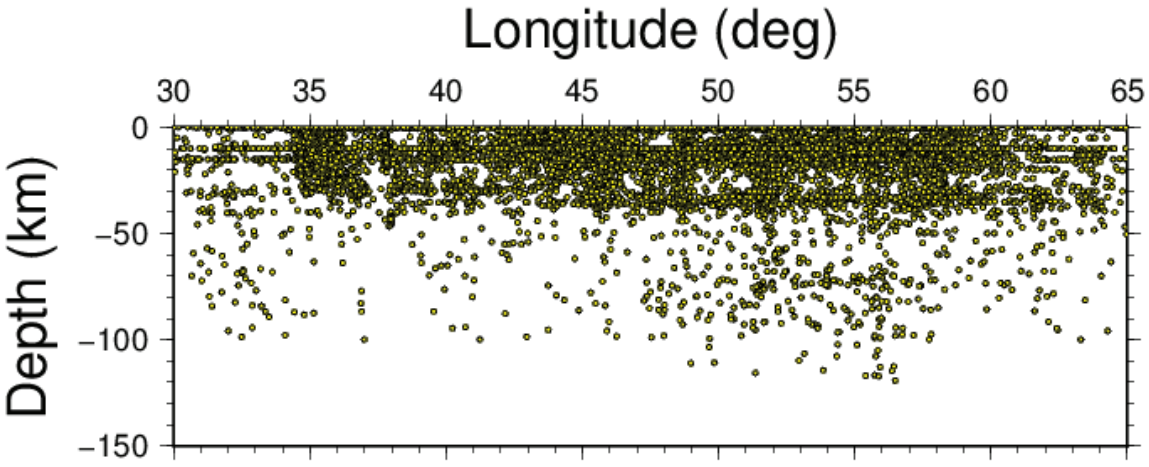

Figure 44. Depth distribution of the events shown in Figure 43 as projected along the longitude direction.

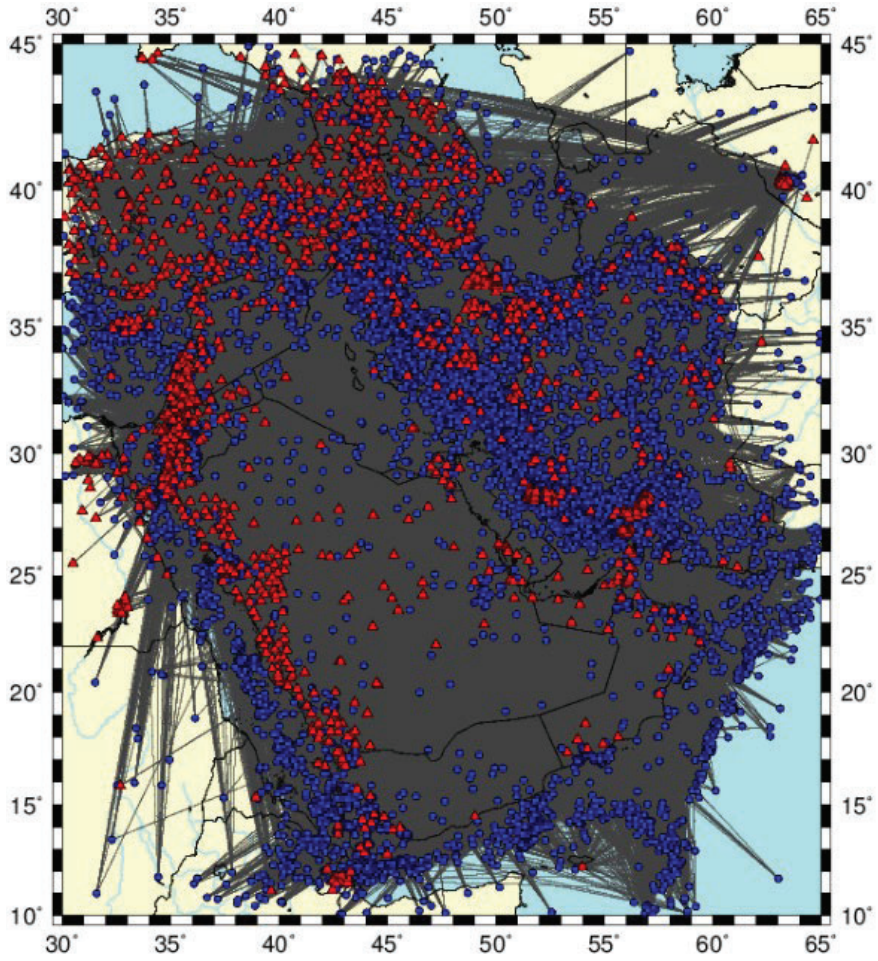

Figure 45. Body wave ray path coverage of the study area in the tomographic inversion. *The red triangles denote the seismic stations and the blue circles the seismic events.*

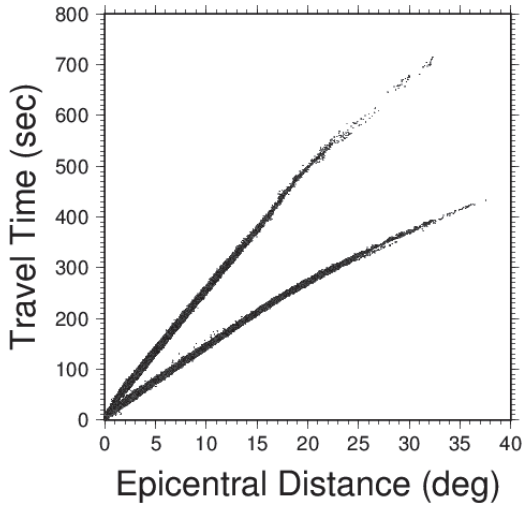

Figure 46. P (lower) and S (upper) wave travel times utilized in the tomographic inversion.

In addition to the body wave travel times, we also adopt Rayleigh wave group velocity dispersions measured in the Middle East. The surface wave data include 95,811 Rayleigh wave group velocity measurements from 256 events recorded by 39 stations in the periods from 2 to 100s. Figure 36 shows ray path coverage of the surface wave data and Figure 37 illustrates the Rayleigh wave group velocity dispersion curves. We also include Rayleigh wave group velocity dispersion measured from ambient noise cross-correlation from 121 station pairs in the region. The weight of the surface wave data is set to 0.1 based the quantity and quality of the data sets following the approach of Fang et al. (2016) [13].

We also include receiver functions obtained at 25 stations in the inversion (Figure 41). To determine the weight of the receiver function data in the inversion, we experiment with various weights and find that the value of 60 gives the optimal balance among the reduction of root-mean-square (RMS) of residuals of individual data sets (Figure 47).

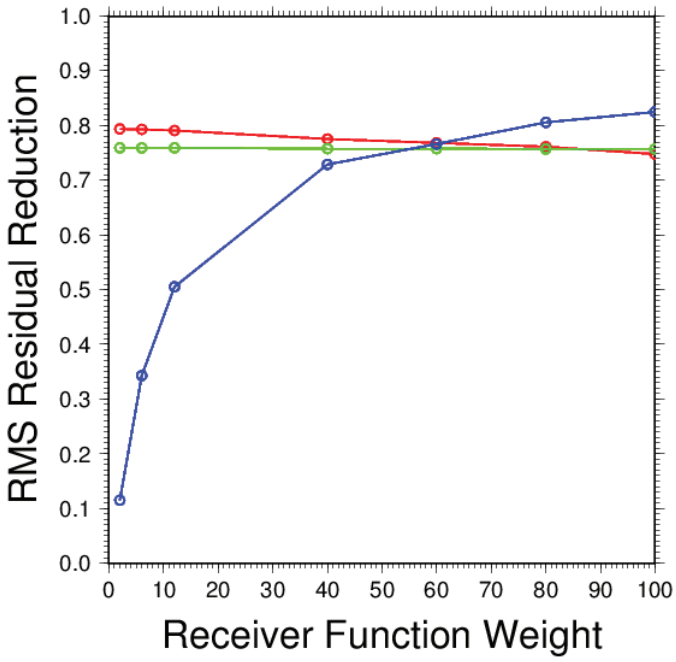

Figure 47. RMS residual reduction for body wave (red), surface wave (green) and receiver function (blue) data with different receiver function weights. *A receiver function weight of 60 is found to have the optimal balance among the individual data sets.*

We determine the smoothing weighting factors in the inversion by running the L-curve tests [24]. Multiple combinations of the weights in three directions are applied in the test runs. Figure 48 shows the results of model variance versus data variance from different combinations of weighting factors. Based on the results of the tests, we conclude that weight combination of 100/100/60 has the optimal balance between model variance and data variance.

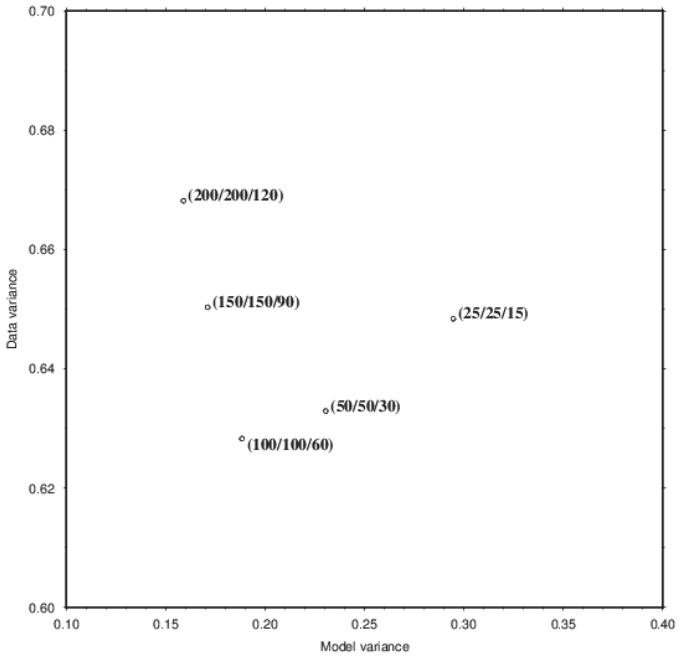

Figure 48. L-curve tests comparing model variance to data variance is used to find the optimal smoothing weighting factors in the tomographic inversion. *The numbers in parenthesis represent weighting factors in X, Y, Z directions, respectively.*

We run the inversion iteratively and invert for velocity models and event relocations simultaneously. The computation stops when the variance reduction becomes insignificant. Figures 49 and 50 present P and S wave velocities at different depths from the inversion. The results show complex features that are in general agreement with the regional tectonics. Noticeably, the Zagros fold belt generally exhibits lower velocity anomalies than the surrounding areas. The Red Sea spreading center has high velocity anomalies. Figure 52a shows P wave velocity along profile A-C indicated in Figure 51. The velocity profile reveals that the Red Sea rift has shallow Moho depth (~10km). The deepest Moho depth along the profile occurs under the Zagros mountains and reaches the depth of 55km. We also plot P-wave velocity along the profile from inversion of body wave travel time data alone in Figure 52b. Although deep structures are similar from both the joint inversion and the inversion of body wave data only, there are noticeable differences between the two at shallow depths. The uplifted Moho discontinuity at the Red Sea rift is clearly revealed by the joint inversion but not well resolved from body wave data alone. Detailed sediment structures are well resolved by the joint inversion. The foreland sediments have noticeably thicker sediment deposits than surrounding areas, reaching the depth of 8km. No sediment is observed in the Arabian Platform. In the contrast, the inversion of body wave data only indicates a uniform distribution of sediments across the area, which is contradicted to findings from various studies in the region. The discrepancies from the two inversions demonstrate the advantage of the joint inversion, especially at resolving shallow structures. We also plot event distribution before and after relocation in the joint tomographic inversion (Figure 53). The relocation after the inversion shows much improved event clustering. Several high dipping-angle earthquake faults in the Zagros fold belt are revealed after the relocation, including the Mountain Front Flexure, High Zagros Fault, and Main Zagros Fault, illustrating the effectiveness of 3D velocity models in high-precision earthquake relocation.

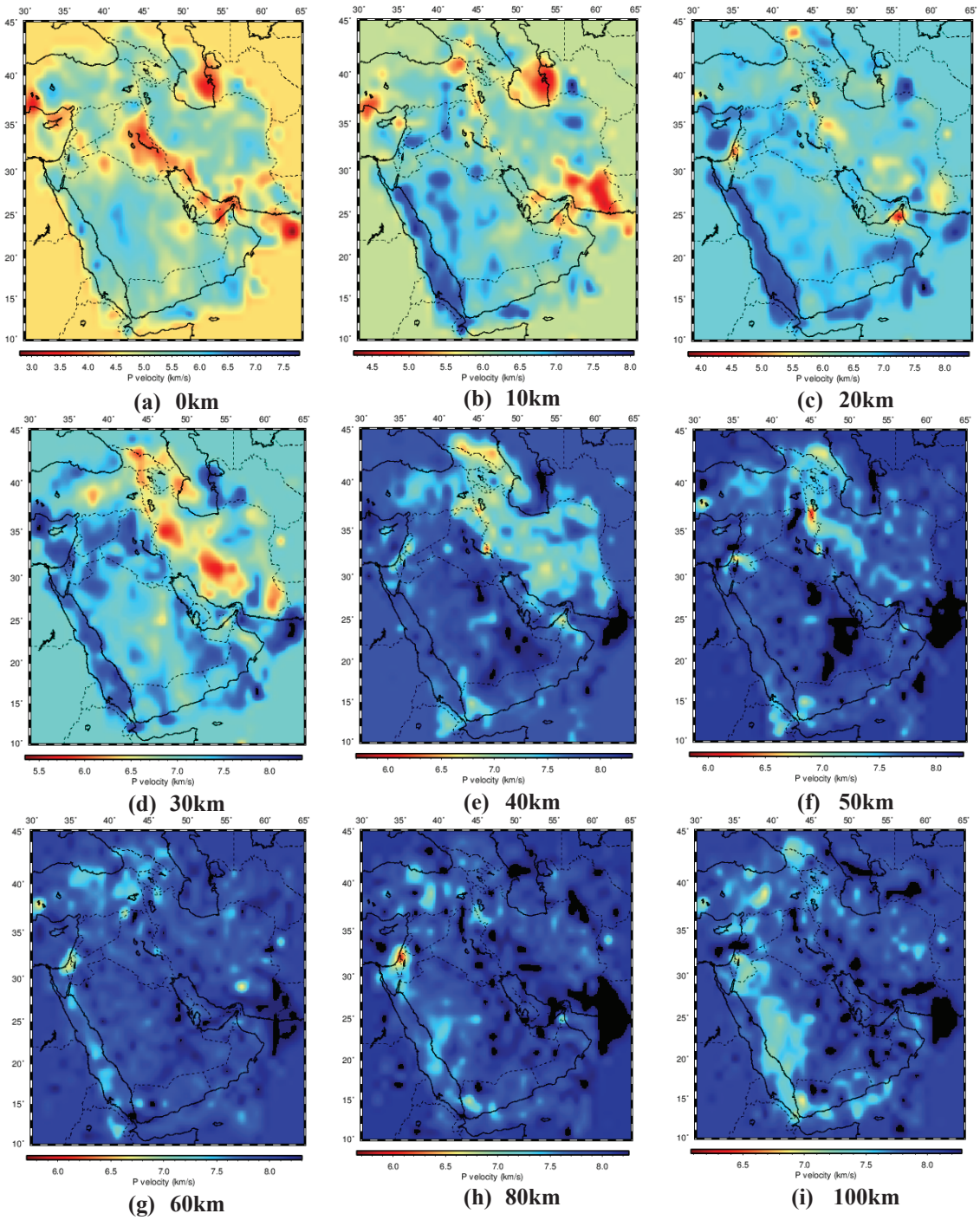

Figure 49. P wave velocities at depths of 0, 10, 20, 30, 40, 50, 60, 80, and 100km, respectively, from tomographic inversion.

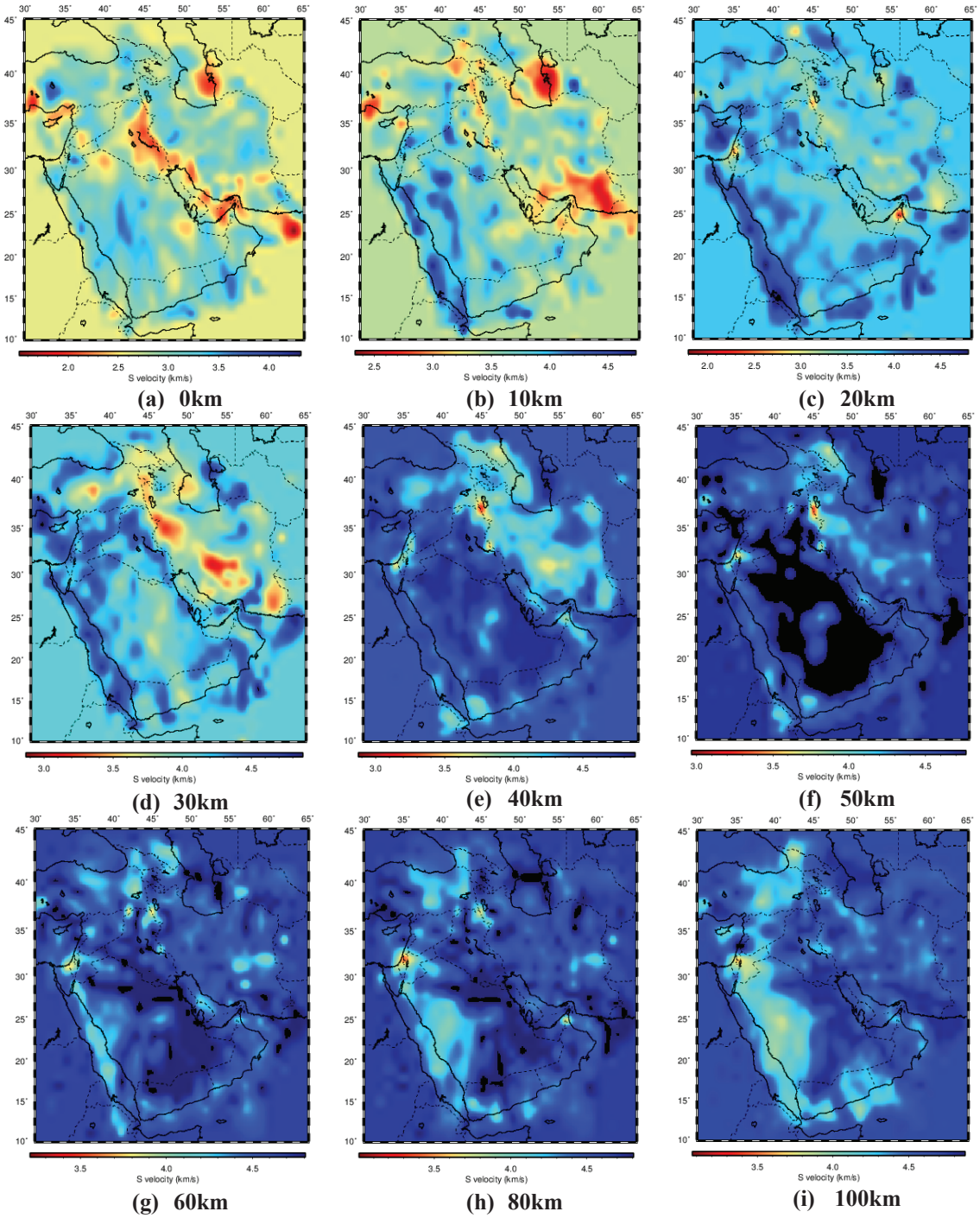

Figure 50. S wave velocities at depths of 0, 10, 20, 30, 40, 50, 60, 80, and 100km, respectively, from tomographic inversion.

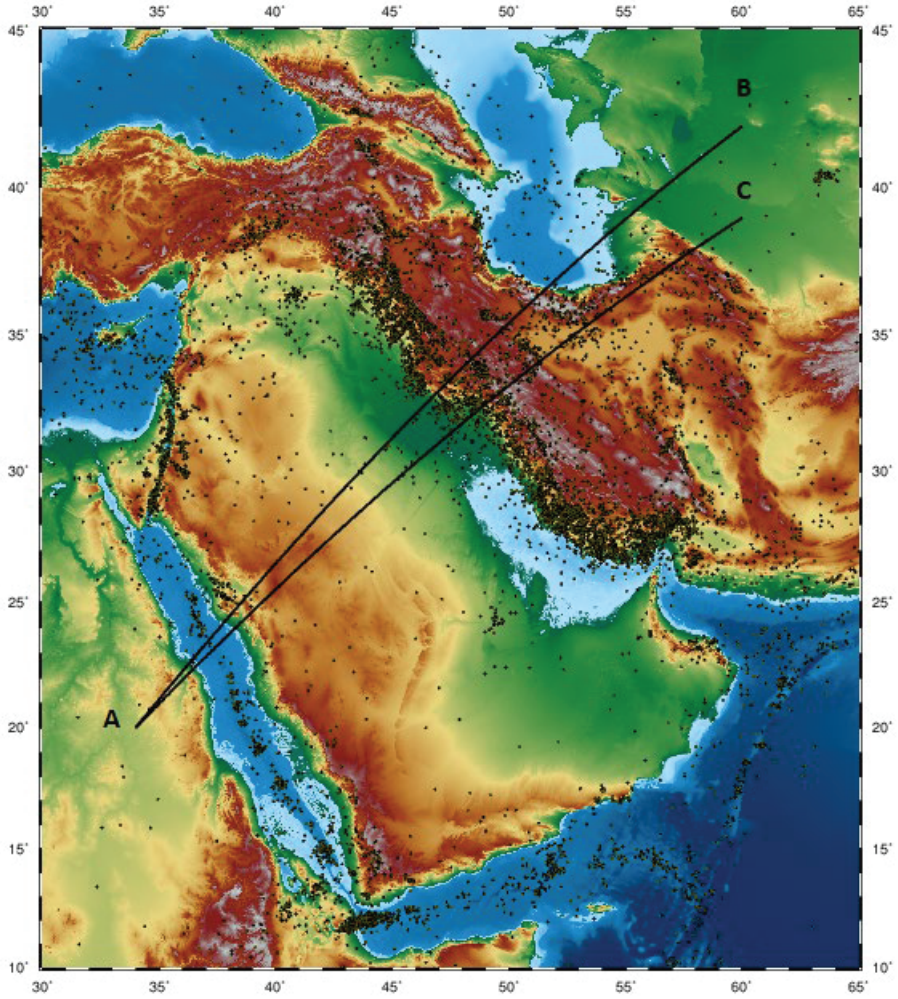

Figure 51. Map showing topography in the Middle East along with earthquakes (dots) in the region. *The lines from A to B and A to C indicate profiles investigated in Figures 52 and 53.*

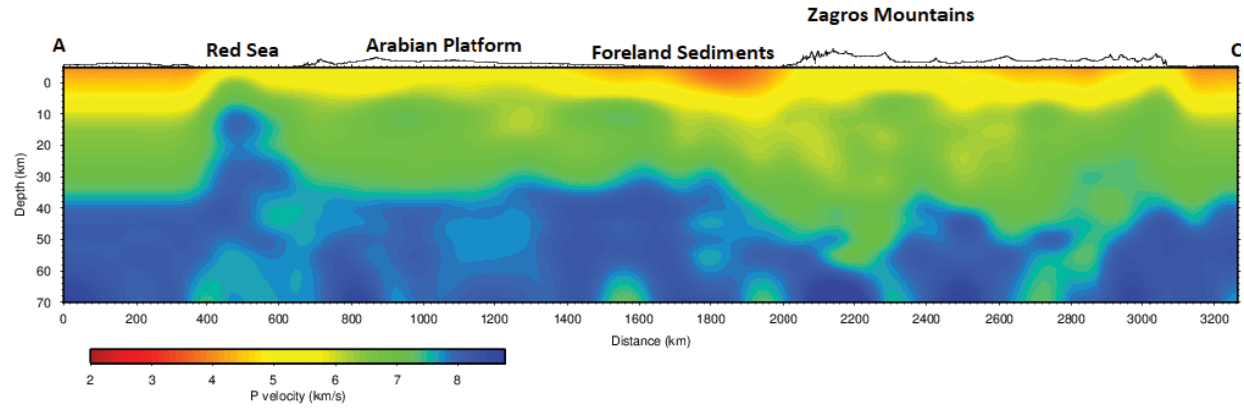

(a)

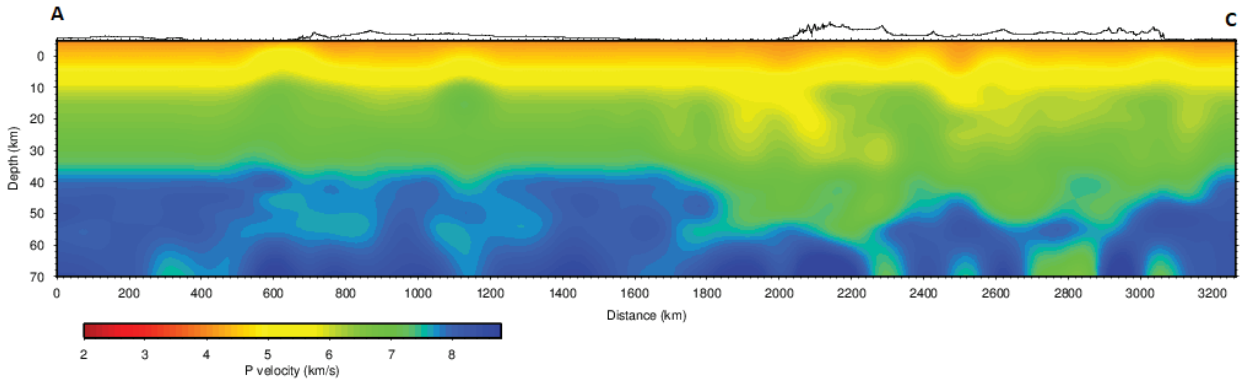

(b)

Figure 52. P wave velocity along profile A-C shown in Figure 51. *(a) from joint inversion of body wave, surface wave and receiver function data; (b) from inversion of body wave data only.*

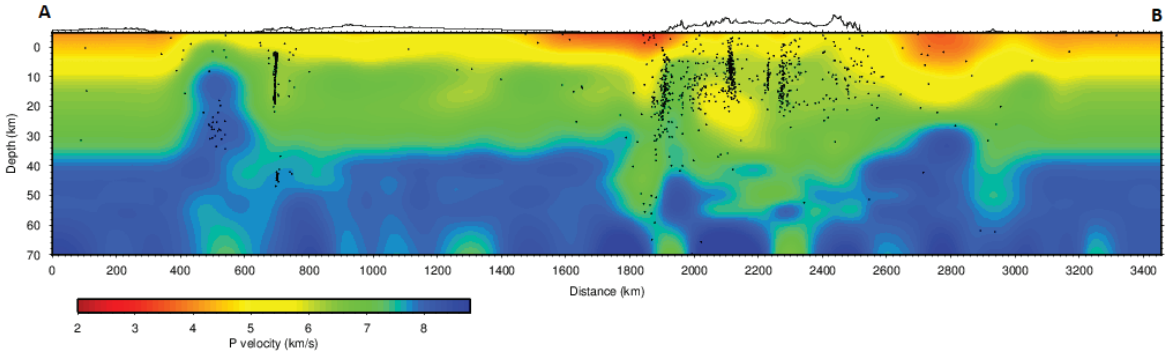

(a)

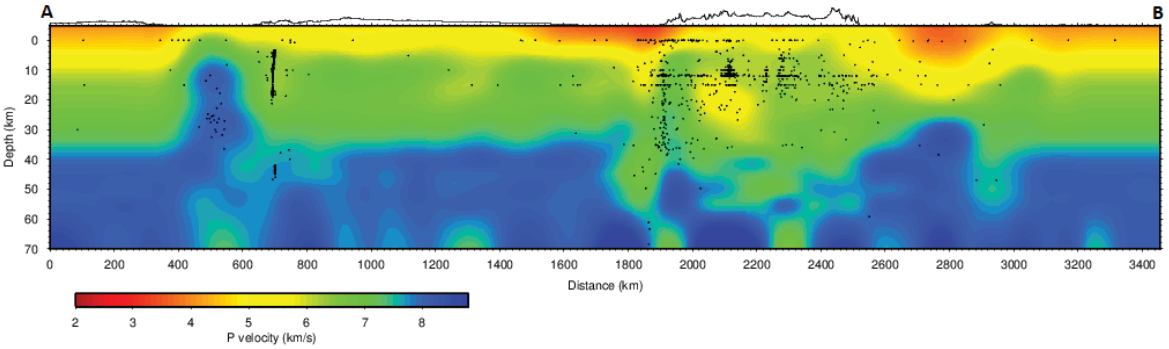

(b)

Figure 53. P-wave velocity and earthquake distribution along profile A-B indicated in Figure 51. *(a) from relocation in tomographic inversion; (b) original earthquake location before relocation.*

5.8. RESOLUTION ANALYSIS FOR TOMOGRAPHIC INVERSION

To evaluate the resolution of the tomographic inversion, we first investigate the derivative weighted sum (DWS) in the inversion which is a measurement of ray density around the inversion nodes. The DWS distribution can be utilized as an indication of the resolution of the obtained velocity model. Figures 54 and 55 show the common logarithm of DWS for P and S waves at various depths of in the inversion. The results indicate that ray densities are sufficient for most of the study area. Along the Zagros Mountains, the DWS has larger values due to the high concentration of seismicity in the tectonic zone. We also conduct checkerboard tests with the body wave, surface wave and receiver function data. In the checkerboard test, we add perturbations from -8% to 8% to the initial velocity model. A forward computation is performed to calculate travel times from the sources to the stations in the perturbed velocity model. The calculated synthetic travel times are then used as input data to the tomographic inversion together with synthetic surface wave and receiver function data obtained in similar ways. The velocity models obtained from the inversion can then be compared to the original perturbed models to gain insights into the resolution of the velocity models from the tomographic inversion. Figure 56 shows P and S velocities at the depths of 0, 30 and 60km from the checkerboard test. The results indicate that the resolution is adequate for most of the study area. In the southern portion of the Arabian Platform, the resolution is less optimal probably because of reduced density of data coverage in the area. The resolution at deeper depth below the crust is not as good as at shallower depth due to the fact that majority of the earthquakes in the region have shallow depths, less than 40km (see Figures 7 and 44).

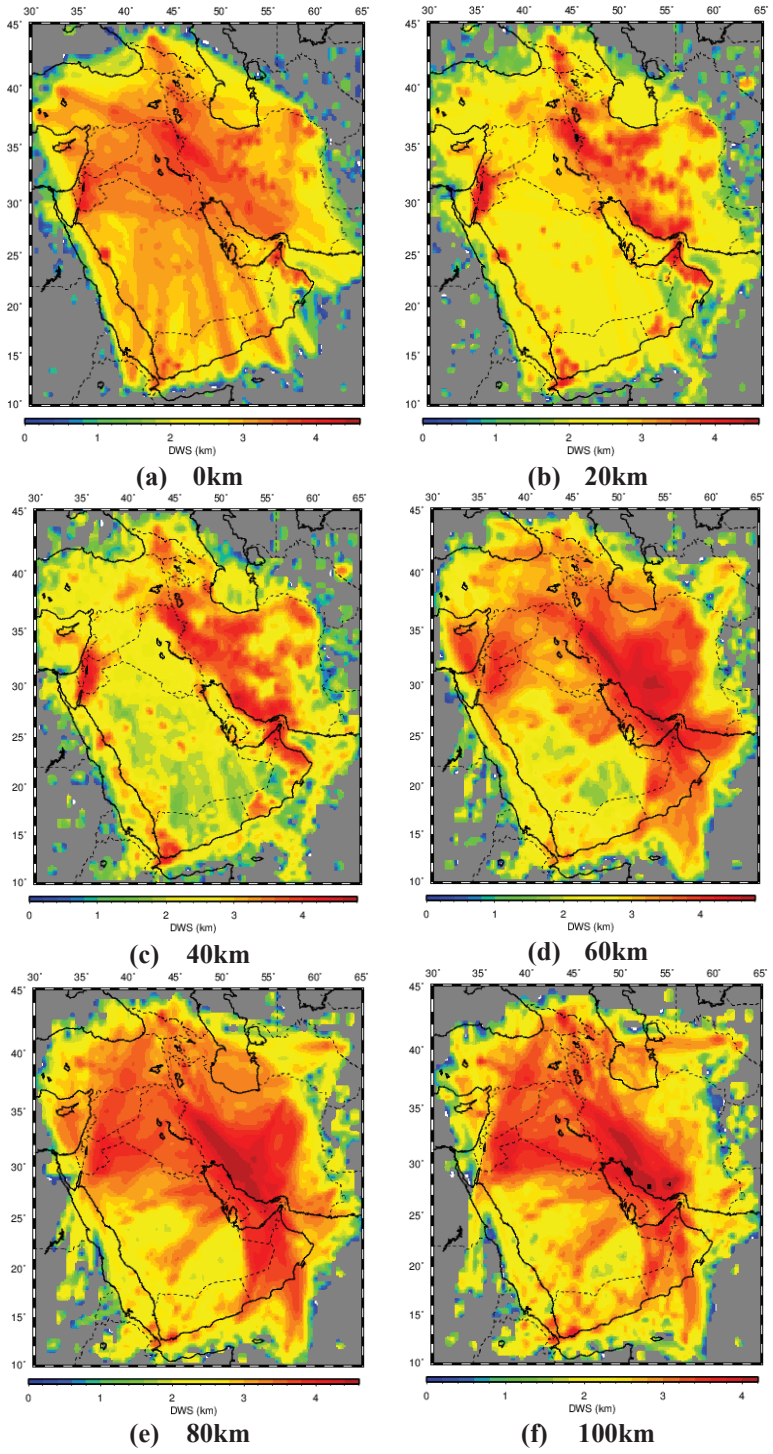

Figure 54. Common logarithm of DWS for P wave at depths of 0, 20, 40, 60, 80, and 100km, respectively, in tomographic inversion.

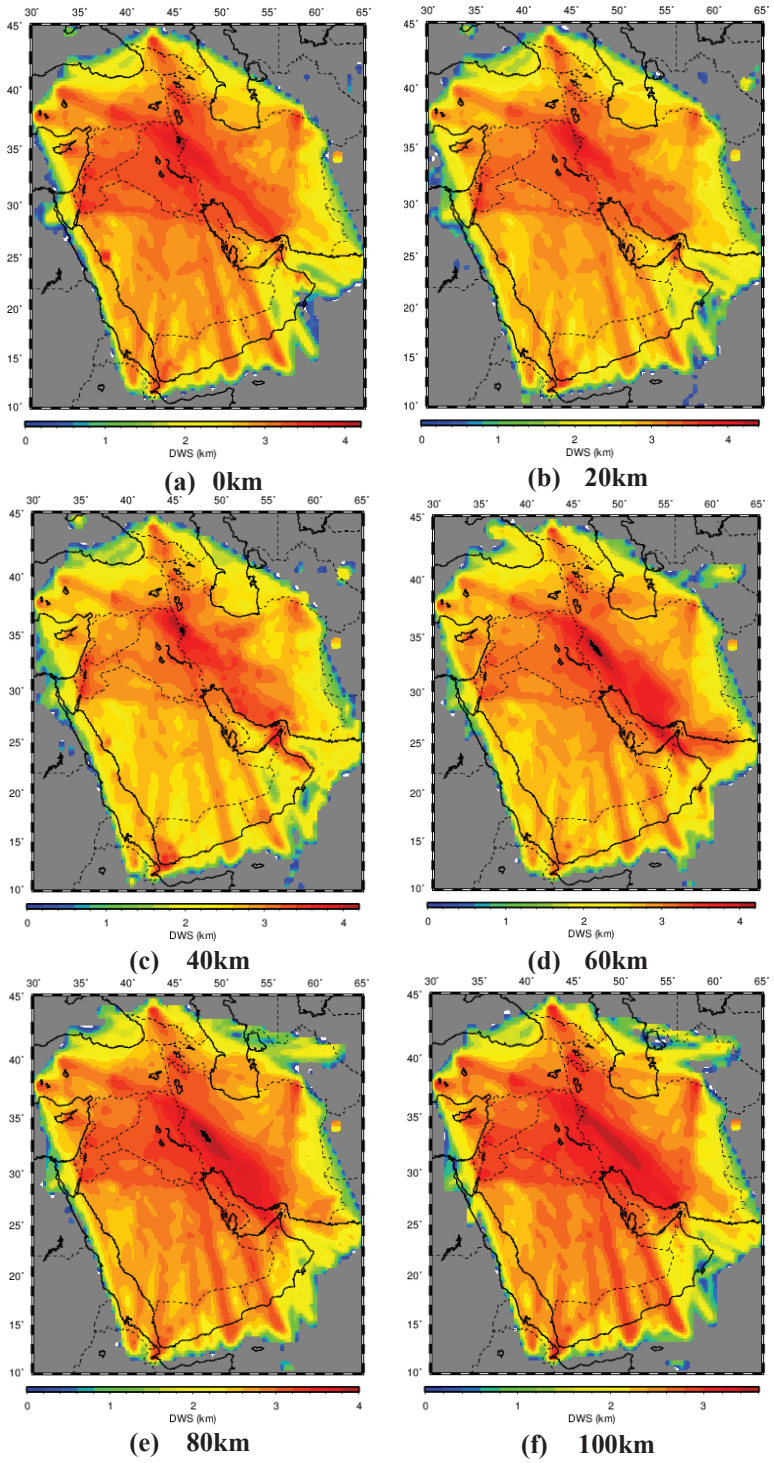

Figure 55. Common logarithm of DWS for S wave at depths of 0, 20, 40, 60, 80, and 100km, respectively, in tomographic inversion.

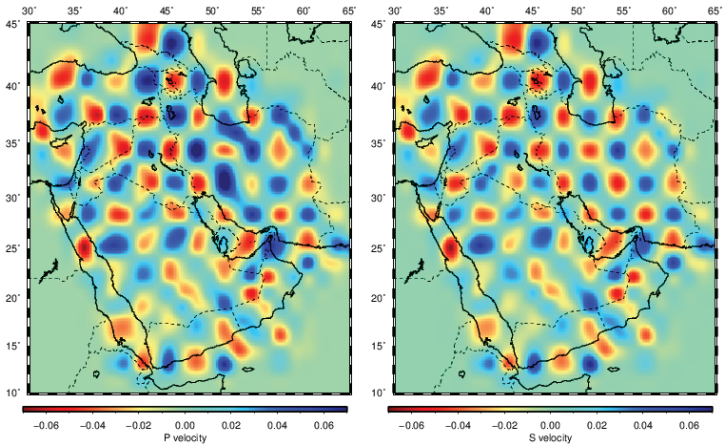

(a) 0km

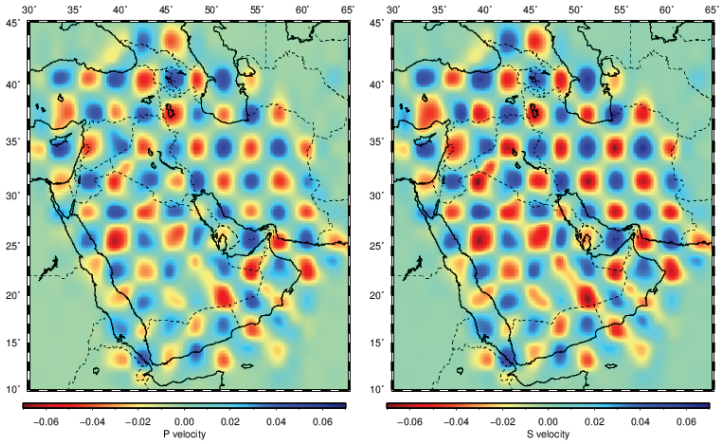

(b) 30km

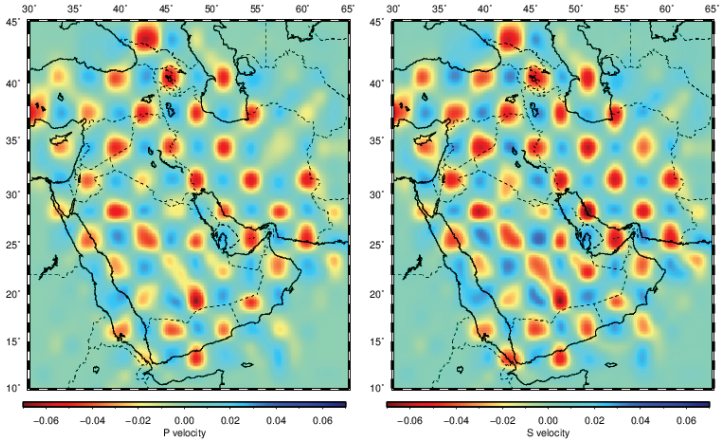

(c) 60km

Figure 56. P and S wave velocities at the depths of 0, 30 and 60km from checkerboard test.

5.9. GT5 DATASET FOR THE MIDDLE EAST

We utilized the event relocations from the tomographic inversion to construct a high-quality ground-truth (GT5) database for the region. Since location uncertainties in earthquake bulletins are often unrealistic, researchers in the calibration community have established criteria to identify candidate GT events. The local network selection criteria for GT5 events developed by Bondár et al. (2004) [37] requires that an event be located by a local velocity model with at least 10 stations, all within 250km, with an azimuthal gap less than 110° and a secondary azimuthal gap less than 160°, as well as with at least one station within 30 km of the epicenter. The latter constraint gives confidence on the depth of the event. The criteria identify GT5 events at the 95% confidence level.

We selected a subset of well-determined seismic events from relocations in the tomographic inversion in the Middle East. The following conditions were applied to the dataset:

1. At least 10 or more recording stations within 250 km epicentral distance.
2. The nearest station at distance <= 30 km.
3. Primary azimuthal gap <= 110 degrees for stations within 250 km.
4. Secondary azimuthal gap <= 160 degrees for stations within 250 km.

We extracted 396 events that satisfy the GT5 criteria of Bondár et al. (2004) [37]. Figure 57 indicates the locations of the GT5 events in the dataset. An example GT5 event that occurred on June 26, 2007 recorded by ten stations in the region is shown in Figure 58. These high-quality GT5 events can be used as a reference dataset to validate regional velocity models and travel time corrections.

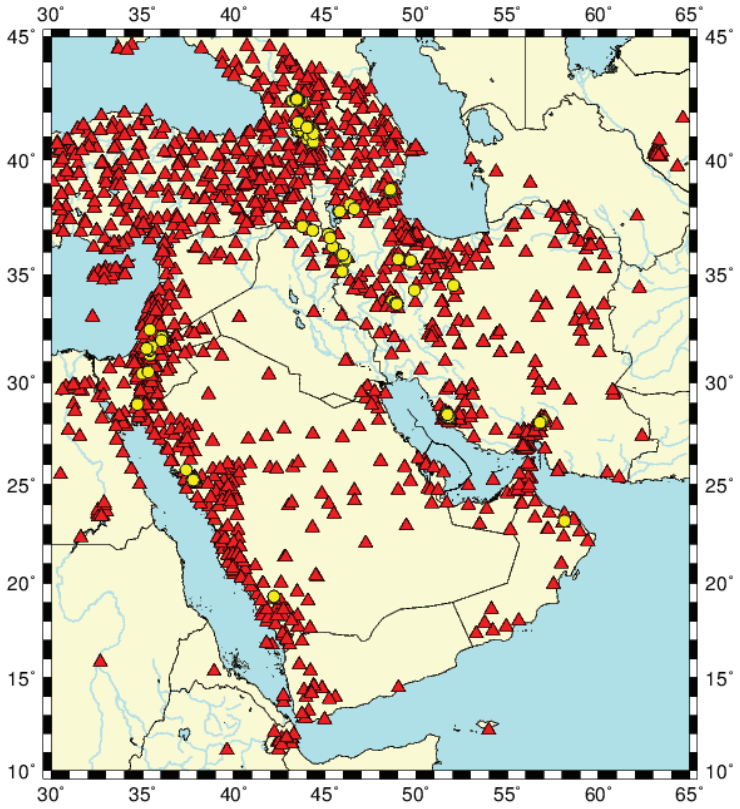

Figure 57. 396 GT5 events in the Middle East are selected using Bondár's criteria [37]. *The yellow circles represent the events and the red triangles the stations.*

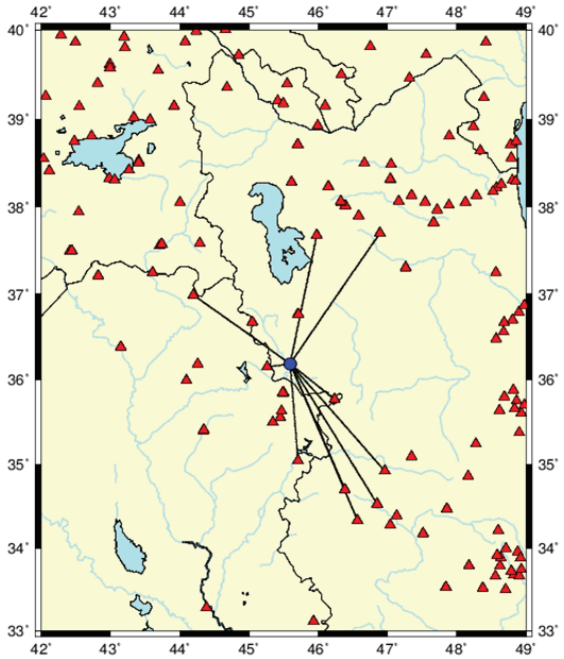

Figure 58. An event (blue circle) in the GT5 dataset that occurred on June 29, 2007 recorded by ten stations (red triangles) in the region.

6. CONCLUSIONS

We have completed processing of 11, 219 events from 2006 to 2010 recorded by deployments and regional seismic networks in the Middle East including the NISN, KSIRS, ISN and IRSC networks. Among the 11,219 seismic events, 5,664 are with magnitudes above 2.0 with the greatest event at magnitude 6.5. The majority of the seismic events occurred at shallow depths of 40km or less. We examine semi-major axes of error ellipses for the relocated events. The maximum population occurs at 5km. 48% of the events have errors less than 10km, and 75% less than 20km. We perform quality control on the phase picks and abnormal arrivals are eliminated to ensure quality of the data. As the double-difference tomography utilizes the first P and S arrivals only, we retain the Pg and Sg arrivals for epicentral distances less than the cross-over distance (set at 2.2° for the study area), and Pn and Sn for epicentral distances greater than the cross-over distance. We have obtained 87,395 P and 69,144 S arrivals of phase picks after quality control. We then reformat the phase picks in a format required by the double-difference tomography software for subsequent tomography study in the region.

To improve coverage of the study area, we have also collected and processed bulletin data from other sources in the Middle East. We retrieved 18 earthquake clusters from the GCCEL database and processed 1,620 seismic events recorded by 1,476 seismic stations in the Middle East. We also processed additional bulletin data from regional seismic networks in the Middle East. We restrict the events and stations in an area with latitudes from 10ºN to 45ºN, and longitudes from 30ºE to 65ºE. The depth is limited to 100km or shallower. To ensure reliability of event locations, we select events in the bulletins that were recorded by at least five stations. Only phase picks with travel time residuals less than 5 seconds are retained to assure quality of the arrival data. We have processed 1,433 seismic events from 2012 to 2016 from seismic networks in Jordan, 18,869 events from 1985 to 2018 from Israel, 20,168 events from 2001 to 2017 from Saudi Arabia, 6,967 events from 2002 to 2013 from Syria, 2,759 events from 2010 to 2016 from UAE, 4,440 events from 2003 to 2016 from Oman, and 2,205 events from 2000 to 2012 from Yemen. These datasets provide supplemental coverage of the study area, especially in the southwestern region, which improves the resolution of subsequent tomography.

We have processed ambient noise data from continuous recordings from the NISN, KSIRS and ISN networks from 2009 to 2010. We perform pre-processing of the continuous data by merging the hourly segments to daily traces and perform quality control on the merged daily data to eliminate errors such as spikes and gaps and malfunctioning of the instruments. We process the ambient noise data including single station data preparation, cross-correlation and temporal stacking, and measurement of dispersion curves. Rayleigh wave phase and group velocity dispersion from 121 pairs of seismic stations are measured in the Middle East. We have also measured surface wave dispersion between earthquakes and stations on seismograms recorded by seismic networks in the Middle East. The MFT technique is adopted to measure Rayleigh wave group velocity dispersions. The procedure includes making instrument response corrections, performing band-pass filtering of multiple bandwidths, calculating energy distribution on the time-frequency domain, and picking the energy peak and a few local maxima at each period. We processed seismic recordings from 256 events from 2001 to 2009 and obtained 2,988 Rayleigh wave group velocity dispersion curves. Quality control is performed on the dispersion data by eliminating abnormal readings.

We have conducted receiver function analysis in the study area. We collect waveforms of teleseismic events recorded by seismic stations in the networks of NISN, KSIRS and ISN at epicentral distances from 30° to 90°. Teleseismic waveforms at additional seismic stations in the study area are also collected from the IRIS, GFZ and ORFEUS data centers to improve the coverage. We first remove the instrument responses. The 3-componet recordings are then rotated to the vertical, radial, and transverse directions. Receiver functions are finally calculated by a time domain iterative deconvolution technique. As P waves from different distances have different incident angles which affects both the time and amplitude of the receiver functions, we correct the receiver functions to a reference slowness of 0.06 deg/s. We then remove the variations due to azimuthal dependence using the "harmonic stripping" technique and stack the receiver functions at each station. Quality checks are performed to eliminate abnormal and low-quality receiver functions. Eventually, receiver functions at 25 stations were obtained and retained through the processing.

With the processed data, we have performed a joint inversion of body wave travel times, surface dispersions and receiver functions for high-resolution P and S velocity models of the Middle East. We utilize absolute body wave travel times, differential body wave travel times, surface wave dispersion between station pairs from ambient noise cross-correlation, surface wave dispersion between station and event pairs from earthquakes, and receiver functions. The study area is set in a region from latitudes 10ºN to 45ºN, and longitudes 30ºE to 65ºE. We divide the study area into 0.5ºx0.5º cells horizontally. In the vertical direction, we set up layers at 5km intervals from the Earth surface to the depth of 60km, and additional layers at 80, 120 and 210km. A 1D starting model is constructed based on previous studies for the crust and the AK135 model for the upper mantle. We select 12,437 events recorded by 1,647 stations from the phase picks database that we have constructed for the region. The body wave data include 178,633 first P arrivals, 70,505 first S arrivals, 100,513 differential P arrivals, and 42,519 differential S arrivals. We also adopt Rayleigh wave group velocity dispersions measured in the Middle East. The surface wave data include 95,811 Rayleigh wave group velocity measurements from 256 events recorded by 39 stations in the periods from 2 to 100s. Rayleigh wave group velocity dispersions measured from ambient noise cross-correlation from 121 station pairs in the region are utilized too. We also utilize receiver functions obtained at 25 stations in the region. We run the inversion iteratively and invert for velocity models and event relocations simultaneously. The obtained velocity models show complex features that are in general agreement with the regional tectonics. Noticeably, the Zagros fold belt generally exhibits lower velocity anomalies than the surrounding areas. The Red Sea spreading center has high velocity anomalies. A velocity profile across the study area reveals that the Red Sea rift has shallow Moho depth of about 10km. The deepest Moho depth in the profile occurs under the Zagros mountains and reaches the depth of 55km. The event relocation after the inversion shows much improved event clustering. Several high dipping-angle earthquake faults in the Zagros fold belt are revealed after the relocation, illustrating effectiveness of 3D velocity models in high-precision earthquake relocations.

We have performed resolution analysis of the tomography results. DWS distribution for P and S waves indicates that ray densities are sufficient for most of the study area. Along the Zagros mountains, the DWS has higher values due to the concentration of seismicity in the tectonic zone. We also conducted checkerboard tests with the body wave, surface wave, and receiver function

data. The checkerboard test results indicate that the resolution of the tomographic inversion is adequate for most of the study area. In the southern area of the Arabian Platform, the resolution is less optimal, probably because of reduced density of data coverage in the area. The resolution at deeper depths below the crust is not as good as at shallower depth due to the fact that majority of the earthquakes in the region have shallow depths, less than 40km.

We have utilized the event relocations from the tomographic inversion to construct a high-quality ground-truth (GT5) database for the region. We extract 396 events that satisfies the GT5 criteria of Bondár et al. (2004) [37]. These high-quality GT5 events can be used as a reference dataset to validate regional velocity models and travel time corrections.

REFERENCES

[1] Smith, G. P. and G. Ekstrom (1996), Improving teleseismic earthquake locations using a three-dimensional Earth model, *Bull. Seismol. Soc. Am.,* 86, pp. 123-132.

[2] Firbas, P. (2000), Location calibration based on 3-D modeling, in *Advances in Seismic Event Location,* C. Thurber and N. Rabinowitz (*eds*), Kluwer, Amsterdam, pp.135-161.

[3] Ritzwoller, M. H., N. M. Shapiro, A. L. Levshin, and G. M. Leahy (2001), Crustal and upper mantle structure beneath Antarctica and surrounding oceans, *J. Geophys. Res*., 106(B12), 30, pp 645-630 and p. 670.

[4] Zhang, H. and C. H. Thurber (2003), Double-difference tomography: The method and its application to the Hayward Fault, California, *Bull. Seismol. Soc. Am*., 93(5), pp. 1875-1889.

[5] Lebedev, S. and R. D. van der Hilst (2008), Global upper-mantle tomography with the automated multimode inversion of surface and S-wave forms, *Geophys. J. Int*., 173(2), pp. 505-518.

[6] Shapiro, N. M., M. Campillo, L. Stehly, and M. H. Ritzwoller (2005), High-resolution surface-wave tomography from ambient seismic noise, *Science*, 307(5715), pp. 1615-1618.

[7] Lin, F.-C., M. P. Moschetti, and M. H. Ritzwoller (2008), Surface wave tomography of the western United States from ambient seismic noise: Rayleigh and Love wave phase velocity maps, *Geophys. J. Int*., 173(1), pp. 281-298.

[8] Picozzi, M., S. Parolai, D. Bindi, and A. Strollo (2009), Characterization of shallow geology by high-frequency seismic noise tomography, *Geophys. J. Int*., 176(1), pp. 164-174.

[9] Shirzad, T. and Z. H. Shomali (2014), Shallow crustal structures of the Tehran basin in Iran resolved by ambient noise tomography, *Geophys. J. Int*., 196(2), pp. 1162-1176.

[10] Woodhouse, J. H. and A. M. Dziewonski (1984), Mapping the upper mantle: Three-dimensional modeling of Earth structure by inversion of seismic waveforms, *J. Geophys. Res*., 89(B7), pp. 5953-5986.

[11] Friederich, W. (2003), The S-velocity structure of the East Asian mantle from inversion of shear and surface waveforms, *Geophys. J. Int*., 153(1), pp. 88-102.

[12] Zhang, H., M. Maceira, P. Roux, and C. Thurber (2014), Joint inversion of body-wave arrival times and surface-wave dispersion for three-dimensional seismic structure around SAFOD, *Pure Appl. Geophys*., 171, pp/ 3013-3022.

[13] Fang, H., H. Zhang, H. Yao, A. Allam, D. Zigone, Y. Ben-Zion, C. Thurber, and R. D. van der Hilst (2016), A new algorithm for three-dimensional joint inversion of body wave and surface wave data and its application to the Southern California Plate Boundary Region, *J. Geophys. Res. Solid Earth*, 121, doi:10.1002/2015JB012702.

[14] Fang, H., H. Yao, H. Zhang, Y.-C. Huang, and R. D. van der Hilst (2015), Direct inversion of surface wave dispersion for three-dimensional shallow crustal structure based on ray tracing: Methodology and application, *Geophys. J. Int*., 201(3), pp. 1251-1263.

[15] Waldhauser F. and W.L. Ellsworth (2000), A double-difference earthquake location algorithm: Method and application to the northern Hayward fault, *Bull. Seism. Soc. Am.*, 90, pp. 1353-1368.

[16] Zhang, H., C.H. Thurber, D. Shelly, S. Ide, G.C. Beroza, and A. Hasegawa (2004), High-resolution subducting slab structure beneath northern Honshu, Japan, revealed by double-difference tomography, *Geology*, 32(4), pp. 361-364.

[17] Koketsu, K. and S. Sekine (1998), Pseudo-bending method for three-dimensional seismic ray tracing in a spherical earth with discontinuities, *Geophysical Journal International*, 132, pp. 339-346.

[18] Zhang, H., and C. Thurber (2006), Development and applications of double-difference seismic tomography, *Pure Appl. Geophys*., 163(2–3), pp. 373-403.
[19] Shapiro, N. M. and M. Campillo (2004), Emergence of broadband Rayleigh waves from correlations of the ambient seismic noise, *Geophys. Res. Lett*., 31, L07614, doi:10.1029/2004GL019491.
[20] Rawlinson, N. and M. Sambridge (2004), Wavefront evolution in strongly heterogeneous layered media using the fast marching method, *Geophys. J. Int*., 156(3), pp. 631-647.
[21] Brocher, T. M. (2005), Empirical relations between elastic wavespeeds and density in the Earth's crust, *Bull. Seismol. Soc. Am*., 95(6), pp. 2081-2092.
[22] Julia, J., C. Ammon, R. Herrmann, and A. M. Correig (2000), Joint inversion of receiver function and surface wave dispersion observations, *Geophys. J. Int*., 143(1), pp. 99-112.
[23] Obrebski, M., R. M. Allen, F. Zhang, J. Pan, Q. Wu, and S.-H. Hung (2012), Shear wave tomography of China using joint inversion of body and surface wave constraints*, J. Geophys. Res*., 117, B01311, doi:10.1029/2011JB008349.
[24] Aster, R. C., B. Borchers, and C. H. Thurber (2011), *Parameter Estimation and Inverse Problems*, 2nd ed., p. 376, Elsevier, Academic Press.
[25] Fong, D. C.-L. and M. Saunders (2011), LSMR: An iterative algorithm for sparse least-squares problems, *SIAM J. Sci. Comput*., 33(5), pp. 2950-2971.
[26] Ammon, C. J. (1991), The isolation of receiver effects from teleseismic P waveforms, *Bull. Seism. Soc. Am.*, v.81, pp. 2504-2510.
[27] Tkalcic, H., M. Pasyanos, A. Rodgers, R. Gok, W. Walter, and A. Al-Amri, (2006), A multi-step approach in joint modeling of surface wave dispersion and teleseismic receiver functions: Implications for lithospheric structure of the Arabian peninsula, *J. Geophys Res*. 111: B11311, doi:10.1029/2005JB004130.
[28] Ghalib, H. A. A., G. I. Aleqabi, B. S. Ali, B. I. Saleh, D. S. Mahmood, I. N. Gupta. R. A. Wagner, P. J. Shore, A. Mahmood, S. Abdullah, O. K. Shaswar, F. Ibrahim, B. Ali, L. Omar, N.I. Aziz, N. H. Ahmed, A. A. Ali, A.-K. A. Taqi, and S. R. Khalaf (2006), Seismic characteristics of Northern Iraq and surrounding regions, in *Proceedings of the 28th Seismic Research Review: Ground-Based Nuclear Explosion Monitoring Technologies*, pp. 40-48.
[29] Ghalib, H., R. Gritto, M. Sibol, R. Hermann, G. Aleqabi, P. Carron, R. Wagner, B. Ali, and A. Ali (2010), A Three-Dimensional Seismic Velocity Model of the Arabian Plate, Iranian and Turkish Plateaus, *Geophysical Research Abstracts*, Vol. 12, EGU2010-7354-2.
[30] Gritto, R., M. Sibol, P. Caron, H. Ghalib, B. Ali, and A. Ali (2011), Investigation of the Crustal Structure in the Middle East from Body-Wave Analysis, in *Proceedings of the 2011 Monitoring Research Review: Ground-Based Nuclear Explosion Monitoring Technologies*, pp. 69-80.
[31] Bensen, G. D., M. H. Ritzwoller, M. P. Barmin, A. L. Levshin, F. Lin, M. P. Moschetti, N. M. Shapiro, and Y. Yang (2007), Processing seismic ambient noise data to obtain reliable broad-band surface wave dispersion measurements, *Geophys. J. Int.,* 169(3), pp. 1239-1260, DOI: 10.1111/j.1365-246X.2007.03374.x.
[32] Yao, H., van der Hilst R.D., and de Hoop, M.V. (2006), Surface-wave array tomography in SE Tibet from ambient seismic noise and two-station analysis: I - Phase velocity maps, *Geophys.J. Int*., Vol. 166(2), pp. 732-744, doi: 10.1111/j.1365-246X.2006.03028.x.
[33] Yao, H. , Xu G., Zhu L.,and Xiao X. (2005), Mantle structure from inter-station Rayleigh wave dispersion and its tectonic implication in Western China and neighboring regions. *Phys. Earth Planet. Inter*., 148(1), pp. 39-54.

[34] Yao, H., Gouedard, P., McGuire, J., Collins, J. and van der Hilst, R.D. (2011), Structure of young East Pacific Rise lithosphere from ambient noise correlation analysis of fundamental- and higher-mode Scholte-Rayleigh waves, *Comptes Rendues Geoscience de l'Académie des Sciences*, 343, pp. 571-583, doi:10.1016/j.crte.2011.04.004.

[35] Shen, W., Ritzwoller, M.H., Schulte-Pelkum, V. and Lin, F.C. (2013), Joint inversion of surface wave dispersion and receiver functions: A Bayesian Monte-Carlo approach. *Geophysical Journal International*, 192, pp. 807-836.

[36] Pasyanos, M. E., W. R. Walter, M. P. Flanagan, P. Goldstein, and J. Bhattacharyya (2004), Building and Testing an a priori Geophysical Model for Western Eurasia and North Africa, *Pure and Applied Geophysics*, 161(2), pp. 235-281.

[37] Bondár, I., S.C. Myers, E.R. Engdahl and E.A. Bergman (2004), Epicenter Accuracy Based on Seismic Network Criteria, *Geophys. J. Int*., Vol.156, No. 3, pp. 483-496.

List of Symbols, Abbreviations, and Acronyms

°	degree
1-D	one-dimensional
3-D	three-dimensional
AK135	one-dimensional average Earth velocity model
AIT	Array Information Technology
CF	cross-correlation function
CSS	Center for Seismic Studies
dB	decibel
DD	double-difference
DWS	derivative weighted sum
E	east longitude
EGF	empirical Green's function
EW	east-west direction
FD	finite-difference
GCCEL	Global Catalog of Calibrated Earthquake Locations
GFZ	German Research Centre for Geosciences
GHz	gigahertz
GPS	Global Positioning System
GSN	Global Seismographic Network
GT5	event locations within 5 km of true location
GUI	graphic user interface
Hz	hertz
IRIS	Incorporated Research Institutions for Seismology
IRSC	Iranian Seismological Center
ISN	Iraq Seismic Network
JSO	Jordan Seismological Observatory
km	kilometers
KSIRS	seismo-acoustic array in north Iraq
Lg	regional seismic surface Love wave
LSMR	an iterative algorithm for sparse least-squares problems

LSQR	an iterative algorithm for sparse least-squares problems
LTA	long-term average
MFT	multiple filter technique
Moho	Mohorovicic discontinuity between the crust and mantle
ML	local magnitude
Ms	seismic magnitude measured from long-period surface waves
N	north latitude
NISN	North Iraq Seismographic Network
NE	northeast
NW	northwest
ORFEUS	Observatories and Research Facilities for European Seismology
P	seismic wave of compressional type
Pg	regional seismic compressional wave confined to the crust
PmP	Moho-reflected regional seismic compressional wave
Pn	regional seismic compressional wave traveling in a waveguide along the Moho
RMS	root mean square
S	seismic wave of shear type
s	seconds
SAC	Seismic Analysis Code
SCEC	Southern California Earthquake Center
sec	seconds
SEFD	spherical-Earth finite-difference
Sg	regional seismic shear wave confined to the crust
S/N	signal to noise ratio
Sn	regional seismic shear wave traveling in a waveguide along the Moho
SNR	signal to noise ratio
sps	sample per second
STA	short-term average
Vp	P-wave velocity
Vs	S-wave velocity
UT	Universal Time

DISTRIBUTION LIST

DTIC/OCP
8725 John J. Kingman Rd, Suite 0944
Ft Belvoir, VA 22060-6218 1 cy

AFRL/RVIL
Kirtland AFB, NM 87117-5776 1 cy

Official Record Copy
AFRL/RVB/Dr. Frederick R. Schult 1 cy

This page is intentionally left blank.